RESEARCH ARTICLE SUMMARY

PHYSIOLOGY

Enterically derived high-density lipoprotein restrains liver injury through the portal vein

Yong-Hyun Han*, Emily J. Onufer, Li-Hao Huang, Robert W. Sprung, W. Sean Davidson, Rafael S. Czepielewski, Mary Wohltmann, Mary G. Sorci-Thomas, Brad W. Warner, Gwendalyn J. Randolph*

INTRODUCTION: High-density lipoprotein (HDL) participates in cholesterol homeostasis and may also have anti-inflammatory or antimicrobial roles through its interaction with numerous plasma proteins. The liver synthesizes most HDL in the body, but the intestine also produces HDL. However, a role for intestinal HDL distinct from that produced by the liver has not been identified. While remodeling its cargo, HDL particles circulate through tissue spaces, but so far, HDL trafficking within tissues has been scarcely studied.

RATIONALE: We reasoned that understanding HDL-trafficking patterns might bring insight into its roles in health and disease, including whether HDL made by the intestine is functionally redundant with that produced by the liver. Using a knock-in mouse that we previously generated to phototag HDL in any tissue location, we aimed to trace the fate of HDL synthesized by the intestine.

RESULTS: Phototagged HDL derived from small bowel enterocytes was generated most abundantly by the ileum and did not travel into draining lymphatic vessels as enterocyte-derived chylomicrons do. Instead, intestinal HDL rapidly entered the portal vein, the major blood supply to the liver. This finding raised the issue of whether the liver might benefit from intestinal HDL and pointed us to an older concept that HDL might neutralize a key microbial signal that can escape a permeable gut: lipopolysaccharide (LPS) from Gram-negative bacteria. Past studies using multiple models have shown that LPS engagement of its receptor, Toll-like receptor 4 (TLR4), in the liver drives significant liver pathology, including inflammation that progresses to fibrosis. Using biochemical, proteomic, and functional approaches, we observed that the intestine produces a particular subspecies of HDL called HDL_3. Unlike another HDL subspecies (HDL_2), HDL_3 sequestered LPS so efficiently that it could not bind to $TLR4^+$ liver macrophages. In this way, HDL_3 produced by the intestine protected the liver from the inflammation and fibrosis observed in a variety of mouse models of liver injury that parallel clinically relevant conditions in humans, including surgical resection of the small bowel, alcohol consumption, or high-fat diets. Administration of an oral drug targeting the transcription factor liver X receptor, the master regulator of genes associated with HDL biogenesis, raised enteric HDL levels and protected the mice from liver pathology. This protection was lost if mice did not express enterically derived HDL, indicating that intestinal HDL was a key target of the drug. Six samples of human portal venous blood with matched systemic venous blood confirmed the enrichment of HDL_3.

Mechanistically, LPS-binding protein (LBP) was enriched in HDL_3 particles and was required for HDL_3 to mask LPS from detection by TLR4. This finding was unexpected because LBP otherwise promotes TLR4 signaling by shuttling LPS to CD14, which then shuttles it to TLR4. Thus, HDL_3 interacts with a known component of the TLR4-signaling platform, LBP, to hide LPS from detection. Without binding to TLR4, the HDL_3-LBP-LPS complex was not retained in liver. Instead, it exited the liver while the LPS associated with it was inactivated. The enzyme acyloxyacyl hydrolase, which is produced in part by liver macrophages and which deacylates critical fatty acid residues in LPS for TLR4 activation, could still access and act upon HDL_3-associated LPS to detoxify it. Low-density lipoprotein bound LPS, but not LBP, and was thus unable to prevent LPS activation of liver macrophages. LBP is in the same family of lipid-binding proteins as phospholipid transfer protein and cholesterol ester transfer protein, which have well-established roles in remodeling the lipid configuration of HDL. Another microbial lipid, lipoteichoic acid from Gram-positive bacteria, is known to bind LBP. We found that it too complexed with HDL_3 and suppressed the activation of liver macrophages.

CONCLUSION: The production of HDL by small bowel enterocytes in a form that potently masks LPS comprises a disease tolerance strategy to protect the liver from injury of enteric origin. Enteric HDL may thus be a suitable pharmacologic target for protecting the liver against gut-derived LPS leakage in alcoholic and nonalcoholic settings. ∎
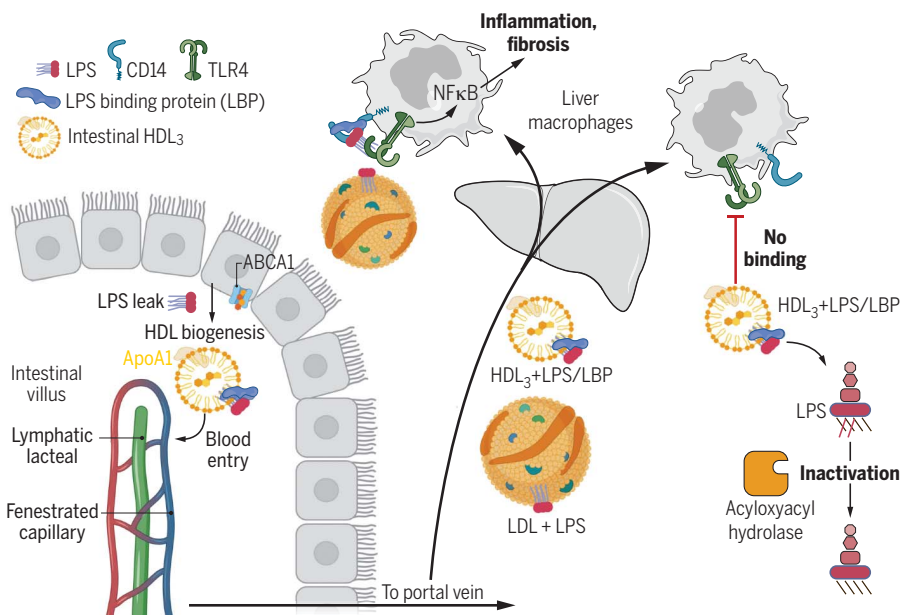

Trafficking and functional properties of enteric HDL. Enterocytes express ABCA1 to promote HDL biogenesis. The nascent HDL enters portal venous blood bearing LBP, which allows it to hide LPS from recognition by $TLR4^+$ macrophages. Failed recognition prevents macrophage activation. Although its ability to trigger macrophages is suppressed by HDL_3, LPS in the HDL_3 complex can still be inactivated by acyloxyacyl hydrolase. Figure was drawn with BioRender.

READ THE FULL ARTICLE AT
https://doi.org/10.1126/science.abe6729

RESEARCH ARTICLE

PHYSIOLOGY

Enterically derived high-density lipoprotein restrains liver injury through the portal vein

Yong-Hyun Han[1,2]*, Emily J. Onufer[3], Li-Hao Huang[1], Robert W. Sprung[4], W. Sean Davidson[5], Rafael S. Czepielewski[1], Mary Wohltmann[1], Mary G. Sorci-Thomas[6], Brad W. Warner[3], Gwendalyn J. Randolph[1]*

The biogenesis of high-density lipoprotein (HDL) requires apoA1 and the cholesterol transporter ABCA1. Although the liver generates most of the HDL in the blood, HDL synthesis also occurs in the small intestine. Here, we show that intestine-derived HDL traverses the portal vein in the HDL_3 subspecies form, in complex with lipopolysaccharide (LPS)–binding protein (LBP). HDL_3, but not HDL_2 or low-density lipoprotein, prevented LPS binding to and inflammatory activation of liver macrophages and instead supported extracellular inactivation of LPS. In mouse models involving surgical, dietary, or alcoholic intestinal insult, loss of intestine-derived HDL worsened liver injury, whereas outcomes were improved by therapeutics that elevated and depended upon raising intestinal HDL. Thus, protection of the liver from injury in response to gut-derived LPS is a major function of intestinally synthesized HDL.

The portal vein collects venous drainage from the intestine, carrying nutrients and metabolites of host and microbiome origin to the liver (1). Through this route, components of the microbiome may drive liver steatohepatitis and fibrosis (2, 3). Enterically derived lipopolysaccharide (LPS) from Gram-negative bacteria triggers Toll-like receptor 4 (TLR4)–dependent injury in the liver after insult to the intestine (3–7).

Mechanisms to limit LPS-mediated liver injury through the gut-portal axis remain incompletely defined. We hypothesized that high-density lipoprotein (HDL) may have an overlooked role in protecting the liver through its potential to neutralize LPS (8–10). Indeed, it is unclear why HDL is synthesized by the intestine rather than solely by the liver. HDL-cholesterol (HDL-C) is the smallest lipoprotein particle in the blood and is best known for its role in cholesterol transport. Only two tissues produce the core protein component of HDL-C, apolipoprotein A1 (apoA1): the liver and the small intestine (11). When intestinal epithelial cells selectively delete the gene encoding the cholesterol transporter ABCA1, which is essential for HDL biogenesis, an ~25% reduction in

plasma HDL-C ensues. Conversely, an ~75% reduction in HDL-C occurs after liver-specific loss of ABCA1 (12), leaving investigators to regard the intestine as simply a second source of HDL-C.

An obstacle to considering a role for intestinal HDL in the gut-liver axis is the paucity of knowledge concerning how enterically derived HDL is delivered to the liver. HDL typically mobilizes from tissues through lymphatic vessels (13–15), which do not route to the liver from the intestine (16). However, an earlier study failed to demonstrate that enterically produced HDL-C entered lymphatics (17). Here, we show that enterically derived HDL-C alternatively traverses portal blood, and that nearly all HDL-C found in the portal vein arises from the intestine. Intestinal epithelial cells produced small HDL particles (HDL_3) (18) with potent LPS-neutralizing properties.

Results

Enterically derived HDL is the main source of HDL in portal blood

Although albumin levels were constant between portal and systemic blood (from the inferior vena cava) (fig. S1A), apoA1 was ~40% lower in portal versus systemic plasma in humans and mice (Fig. 1A). To determine whether this reduction resulted from diminished recirculation of HDL into portal blood, we traced HDL using photoactivatable green fluorescent protein (GFP) apoA1 knock-in mice ($Pga1^{KI/+}$) (15). When phototagged in the skin, HDL appeared in systemic blood but was very low in portal blood (Fig. 1B). Its appearance in mesenteric lymph to a concentration approaching that in the systemic circulation (Fig. 1B) suggested that it left the bloodstream to access lymph before entering the portal vein (Fig. 1B).

Within 5 min after phototagging HDL in the small intestinal lumen, fluorescence was strong in portal blood but not lymph (Fig. 1C). By 30 min, these compartments equilibrated (Fig. 1C). HDL phototagged along the intestinal exterior appeared in lymph but not portal blood (Fig. 1D). These patterns were unaffected by dietary composition or fasting (fig. S1, B to D). Thus, HDL tagged at the intestinal epithelium first enters the portal vein and is not observed in lymph until cargo in the portal vein passes through the liver and enters the systemic circulation. Upon reapproaching the gut, it appears to traverse into the interstitium and then into lymph.

Separate phototagging of the duodenum, jejunum, and ileum revealed the ileum as the major site of enteric HDL biogenesis (Fig. 1E). Like apoA1, HDL-C in portal plasma of humans or mice was present at lower concentrations than in systemic blood (Fig. 1F). HDL-C was decreased by >75% in portal blood of intestine-specific ABCA1-knockout mice ($Vil1^{Cre}$-$Abca1^{fl/fl}$; $Abca1^{ΔVil1}$) (Fig. 1G). However, in systemic blood of $Abca1^{ΔVil1}$ mice, HDL-C dropped by only 25% (Fig. 1H) (12). By contrast, a marked reduction of HDL-C in systemic but not portal blood was observed in liver-specific ABCA1-knockout mice ($Alb1^{Cre}$-$Abca1^{fl/fl}$; $Abca1^{ΔAlb1}$) (Fig. 1, G and H). Thus, two distinct blood compartments for HDL exist: one entering the portal drainage governed by intestinal production of HDL and the other in systemic vessels governed by liver production of HDL.

Portal blood HDL is mainly HDL_3 and strongly suppresses Kupffer cell inflammatory responses

Portal venous HDL was relatively small in size (~8 nm) in humans (Fig. 2A) and mice (Fig. 2B), suggestive of a subspecies of HDL called HDL_3. Small-sized HDL_3 and large-sized HDL_2 particles carry distinct accessory proteins, with paraoxonase 1 (PON1) enriched in the former and apoB in the latter (18). Thus, we compared HDL_2 or HDL_3 species separated by ultracentrifugation from pooled human systemic blood with that of the larger or smaller HDL species from portal or systemic blood isolated by size-exclusion fast protein liquid chromatography (FPLC) and affinity purification (Fig. 2C). This approach yielded four samples from the same individual, putative HDL_2 and HDL_3, each from both systemic and portal blood, allowing evaluation of how venous location affects HDL composition. Proteomic analysis revealed >250 proteins in each sample. A heatmap depicting relative abundance of proteins revealed that small-portal venous HDL shared a protein profile with HDL_3 from human systemic blood (Fig. 2D and table S1). Similarities included known enrichments of PON1, PON3, $α_1$-antitrypsin (SerpinA1), and PLTP in all HDL_3 fractions regardless of portal or systemic blood origin

[1]Department of Pathology, Washington University School of Medicine, St. Louis, MO 63110, USA. [2]Laboratory of Pathology and Physiology, College of Pharmacy, Kan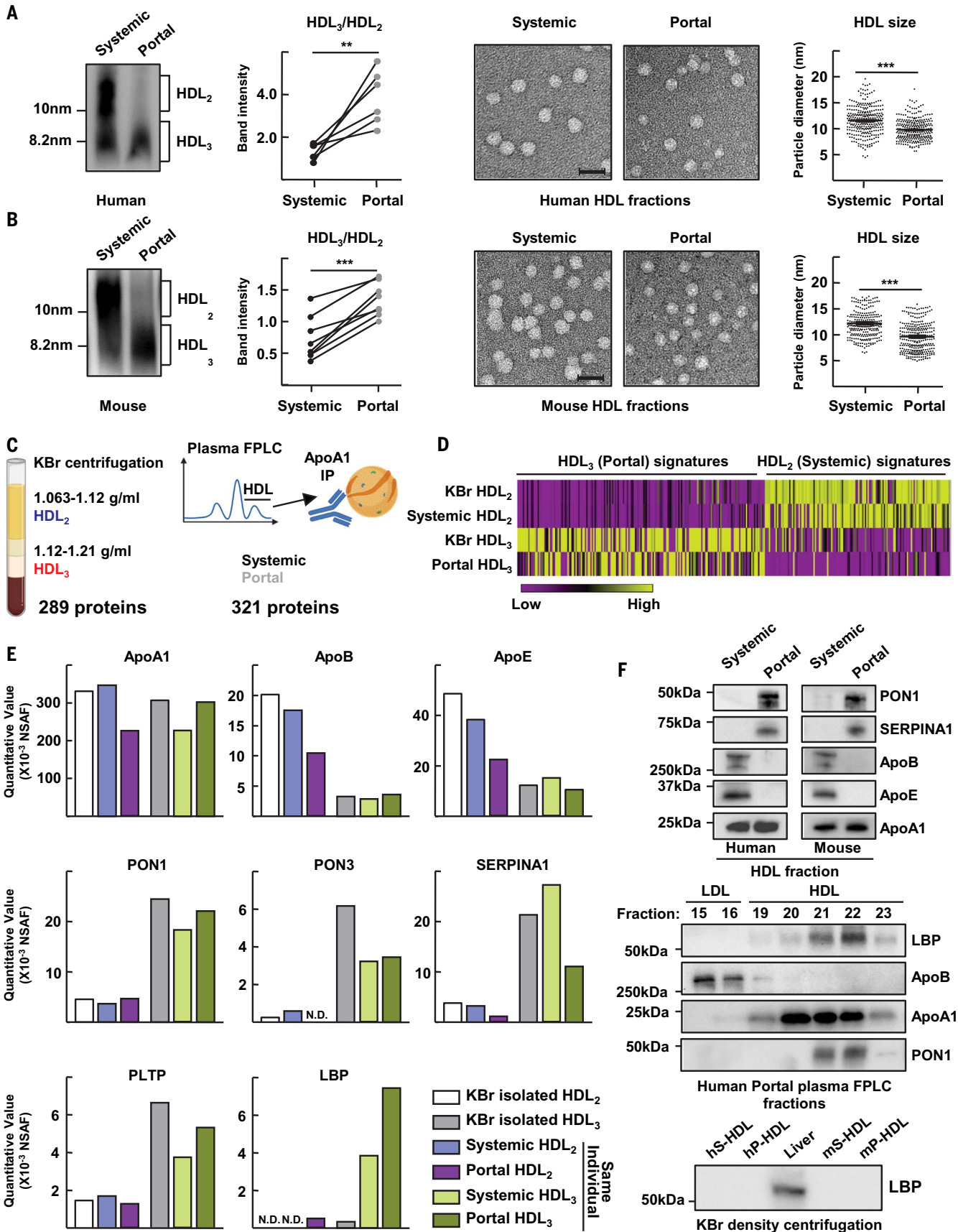gwon National University, Chuncheon 24341, South Korea. [3]Department of Surgery, Washington University School of Medicine, St. Louis, MO 63110, USA. [4]Department of Medicine, Washington University School of Medicine, St. Louis, MO 63110, USA. [5]Department of Pathology and Laboratory Medicine, University of Cincinnati, Cincinnati, OH 45237, USA. [6]Department of Medicine, Division of Endocrinology, Pharmacology and Toxicology, and Blood Research Institute, Medical College of Wisconsin, Milwaukee, WI 53226, USA.

*Corresponding author. E-mail: gjrandolph@wustl.edu (G.J.R.); yhhan1015@kangwon.ac.kr (Y.-H.H.)
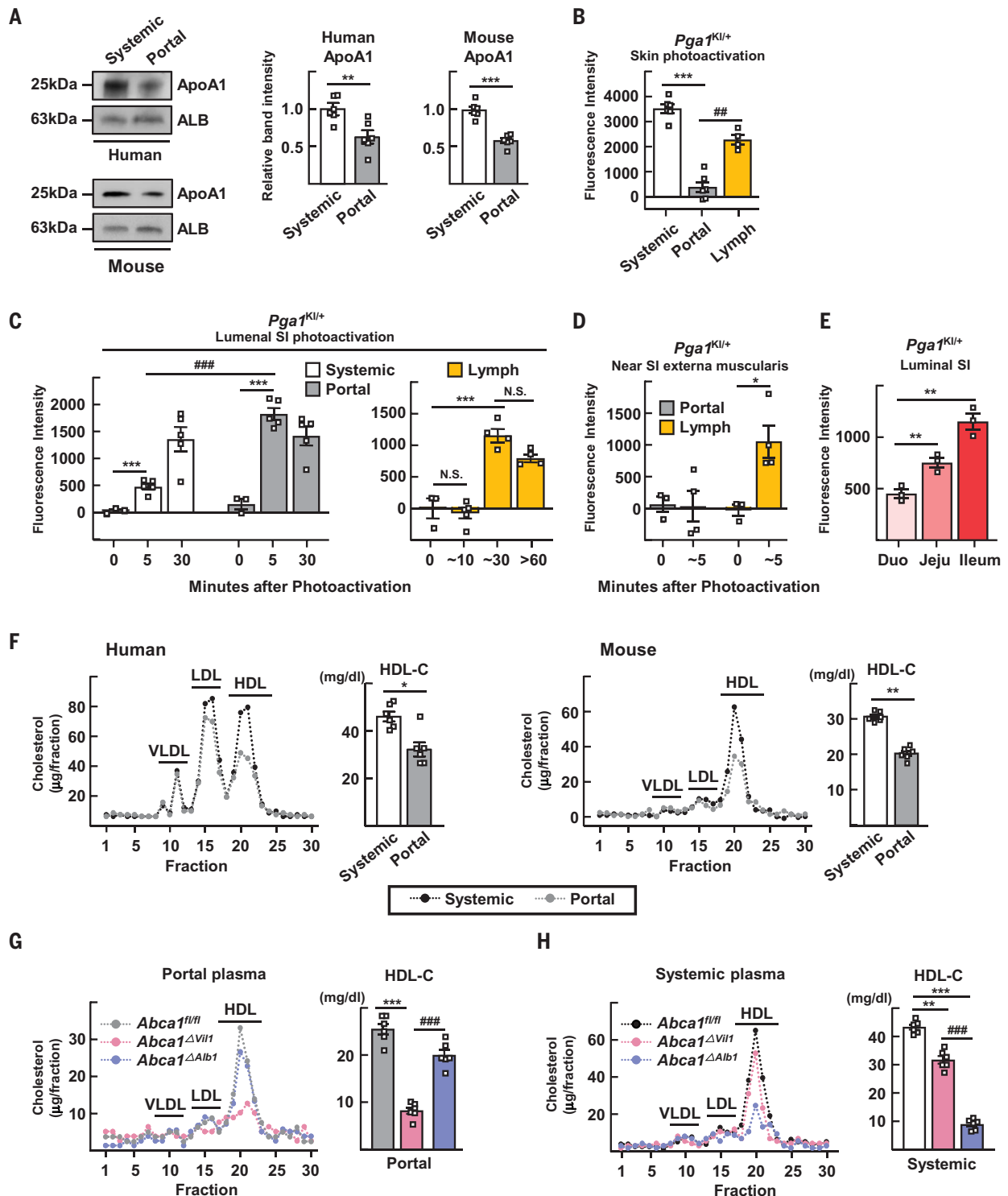
Fig. 1. Intestinal HDL transits through the portal vein and accounts for most of the HDL in the portal blood. (**A**) Immunoblot for apoA1 in systemic and portal serum from humans and mice. ALB, albumin. (**B**) Plasma and lymph fluorescence measured 2 hours after phototagging HDL in skin. (**C** and **D**) Portal plasma and mesenteric lymph fluorescence after phototagging the lumen (C) or externa muscularis (D) of the small intestine (SI) of *Pga1*^KI/+ mice. (**E**) HDL phototagged in different small bowel regions separately. (**F**) Lipoprotein profiles from humans fasted overnight or mice fasted for 4 hours. (**G** and **H**) Lipoprotein profiles and HDL-C quantification of portal (G) or systemic (H) plasma after 4 hours of fasting. Plots show mean ± SEM. (A) and (F) show paired data from six human subjects or six WT mice (same subjects in both panels). (B) to (E) show data for 65 *Pga1*^KI/+ mice. Each symbol designates different mice, except that systemic versus portal blood in (B) and systemic versus portal blood from the same time points in (C) were from the same mice (paired). Most panels show one experiment, except for (C), which combines two experiments. (G) and (H) show five individual mice from each of three genotypes from one experiment, with paired portal (G) and systemic (H) plasma within the same genotype. *$P < 0.05$, **$P < 0.01$, ***$P < 0.001$, ##$P < 0.01$, ###$P < 0.001$. Data in (A) and (F) were analyzed for statistical significance using a paired *t* test; data in all other panels were analyzed using one-way ANOVA.

Fig. 2. Portal vein HDL is enriched in small HDL$_3$ particles. Samples (from Fig. 1A) of systemic or portal plasma from humans (**A**) or mice (**B**) immunoblotted for apoA1 after electrophoresis under nondenaturing conditions. Representative gels and plots show HDL$_3$/HDL$_2$ ratios in six paired samples. Also shown are representative electron microscopy images of negative-stained HDL fractions. Scale bars, 20 nm. HDL diameter measurements, plotted as individual symbols, combine assessments from four of six humans or mice (right). For proteomics (**C** to **F**), density ultracentrifugation-purified HDL$_2$ or HDL$_3$ yielded 289 associated proteins (C, left). Size-exclusion FPLC with immunopurified HDL identified 321 proteins (C, right). This experiment was performed once using four paired samples derived from the same individual (HDL$_2$ or HDL$_3$ from two vascular beds). Additional samples were HDL$_2$ or HDL$_3$ from commercially available pooled human plasma isolated by density ultracentrifugation. (D) Heatmap of protein abundance. (E) Normalized spectral abundance factor plotted for selected proteins. (F) Select proteins immunoblotted from portal or systemic plasma HDL (top), using indicated fraction numbers collected after FPLC separation (middle). Immunoblot of LBP from human or mice systemic (hS- and mS-) and portal (hP- and mP-) plasma or whole liver lysate (bottom). LBP quantification is shown in fig. S2A. N.D., not detected. **P < 0.01, ***P < 0.001. Paired t test was used for statistical evaluation in (A); unpaired t test was used in (B).

or method of isolation (Fig. 2E). Some proteins, such as LPS-binding protein (LBP), were especially enriched in immunopurified portal blood HDL$_3$ but notably absent after ultracentrifugation (Fig. 2E). The distribution of LBP was confirmed by immunoblotting of the FPLC fractions used to purify HDL$_2$ (fraction 20) versus HDL$_3$ (fraction 22) from human portal vein (Fig. 2F), systemic blood (fig. S2), or murine portal blood (fig. S2). When these serum samples were subjected to HDL isolation using ultracentrifugation, LBP was absent (Fig. 2F), suggesting its dissociation during ultracentrifugation (19).

Because LBP delivers LPS to CD14 to facilitate TLR4 signaling (20), we investigated whether the association of portal venous HDL$_3$ with LBP affects LPS signaling. We isolated primary liver Kupffer cells (KCs) (21, 22) (fig. S3A) from wild-type (WT) or Tlr4$^{-/-}$ mice, and observed that portal vein–derived HDL from humans or mice neutralized LPS-induced proinflammatory responses in these cultures more effectively than HDL from systemic blood or no HDL at all (Fig. 3, A and B). Whole portal plasma obtained from Abca1$^{\Delta Vil1}$ mice less effectively protected against induction of inflammation (Fig. 3C), implicating gut-derived HDL in this activity. Similarly, comparison of human HDL$_2$ or HDL$_3$ from human peripheral blood showed that HDL$_3$ more strongly suppressed LPS-induced inflammatory genes (Fig. 3D) than HDL$_2$ in a concentration-dependent, TLR4-dependent manner (Fig. 3D). Activation of KCs by lipoteichoic acid was also robust and strongly blocked by HDL$_3$. CpG oligodeoxynucleotides stimulated KCs less strongly, but HDL$_3$ did have some inhibitory effect (fig. S3B). Modest inhibition was observed when the cytokines interleukin 1β (IL-1β) or tumor necrosis factor (TNF) were used to induce inflammatory activation of KCs (fig. S3C). In these assays (Fig. 3, A to D), LBP was included as an exogenous additive to restore the LBP removed during centrifugation. Excluding LBP abrogated the anti-inflammatory effects of HDL$_3$ (Fig. 3E). Similarly, HDL$_3$ suppressed LPS bioactivity but only in the presence of LBP (Fig. 3F). Thus, portal blood HDL$_3$ inhibits LPS signaling in TLR4$^+$ macrophages in an LBP-dependent manner.

Portal HDL$_3$ efficiently binds LBP and LPS to prevent LPS binding to KC TLR4

We next evaluated binding between HDL and LPS using LPS conjugated with biotin at its inner core (23–25). HDL$_3$ more robustly bound LPS compared with HDL$_2$, but the presence of LBP was required (Fig. 4A). HDL$_2$-bound LPS readily transferred to low-density lipoprotein (LDL) or very-low-density lipoprotein (VLDL), whereas most HDL$_3$-bound LPS remained associated with HDL$_3$ (Fig. 4B). In an immuno-absorption assay, HDL$_3$ was indeed shown to be more effective than HDL$_2$ and LDL in binding LBP (Fig. 4C), and LDL did not compete (Fig. 4, C and D). LDL bound LPS efficiently (Fig. 4D) but did not bind LBP (Fig. 4C). LDL did not neutralize LPS bioactivity (Fig. 4E), nor did it dampen inflammatory gene expression (fig. S4A) with or without LBP (Fig. 4E). Reconstituted HDL also did not neutralize LPS (Fig. 4E). In the presence of LBP, interactions between biotin-LPS and HDL$_3$ generally reduced the detection of biotin-LPS by streptavidin capture (Fig. 4F). This reduction was caused by efficient masking of the inner core biotin label of LPS, because disruption of HDL$_3$ with detergent reexposed the biotin (Fig. 4F). Thus, binding of LBP to HDL$_3$ promotes the sequestration of LPS.

To determine whether HDL$_3$ sequesters LPS from KCs, we cocultured KCs with biotin-LPS and monitored surface binding (Fig. 4G). This binding largely depended upon TLR4 (Fig. 4H) and was unaffected by the absence or blockade of lipoprotein or scavenger receptors (fig. S4B). HDL$_3$ robustly prevented LPS interaction with KCs but only in the presence of LBP. Reconstituted HDL (Fig. 4G) or LDL in the presence or absence of LBP (fig. S4C) did not diminish binding, whereas HDL$_2$ partially blocked it (Fig. 4G). Peak interaction occurred within 3 hours of incubation with KCs (Fig. 4I). Substantial internalization of biotin-LPS by macrophages in the presence or absence of HDL$_3$ was not detected during this time (fig. S4D).

We next wondered whether, after failing to bind to cells, LPS associated with HDL$_3$ might later be inactivated. Using a low dose of HDL$_3$ (20 μg/ml) that only weakly suppressed LPS activity in a cell-free system (Fig. 3F), we observed that LPS activity was further lowered in the presence of macrophages or macrophage supernatant. This was true as long as the KCs were not held at 4°C (Fig. 4J), suggesting that a soluble product from KCs inactivated LPS. The enzyme acyloxyacyl hydrolase (AOAH), which is produced in part by KCs, deacylates and thereby inactivates LPS (26). Depletion of AOAH from KC-conditioned medium increased the recovery of LPS bioactivity (Fig. 4K). Because AOAH would not remove the biotin from the inner core of LPS upon deacylation, we calculated LPS bioactivity normalized to recovered biotin after disrupting HDL$_3$ with detergent, finding that AOAH indeed drove inactivation of HDL$_3$-bound LPS (Fig. 4L). We performed a similar experiment in vivo, injecting a constant dose of biotin-LPS into the portal vein in complex with HDL$_3$, HDL$_2$, or LDL. After 30 min, when enterically derived HDL had passed through the liver to access the systemic circulation (Fig. 1C), we drew systemic venous blood to recapture and assess LPS. More of the recovered LPS was inactive when complexed with HDL$_3$ than with HDL$_2$ or LDL (Fig. 4M and fig. S4E), indicating the inactivation of HDL$_3$-associated LPS. The administration of LPS-loaded lipoproteins into the portal vein caused acute elevation in aspartate aminotransferase (AST), a measure that was lowest when HDL$_3$ was the vehicle carrying LPS and highest when LDL carried LPS (fig. S4F). Thus, HDL$_3$ masks LPS to limit inflammation by blocking LPS binding to KCs, but HDL$_3$-associated LPS remains susceptible to inactivation by AOAH, allowing its permanent inactivation.

The LPS receptor TLR4 on KCs drives liver injury and fibrosis

To determine whether HDL neutralization of LPS modulates liver inflammation in vivo, we studied a model of small bowel resection that promotes marked liver fibrosis (27, 28). Small bowel resection removed 50 or 75% of the small intestine (Fig. 5A), sparing the proximal part of the small intestine and the terminal ileum except when indicated otherwise. Within 3 months, these resections induced morphological changes in the liver (Fig. 5B), elevated the plasma AST (Fig. 5C), and enhanced the infiltration of myeloid cells (F4/80$^+$
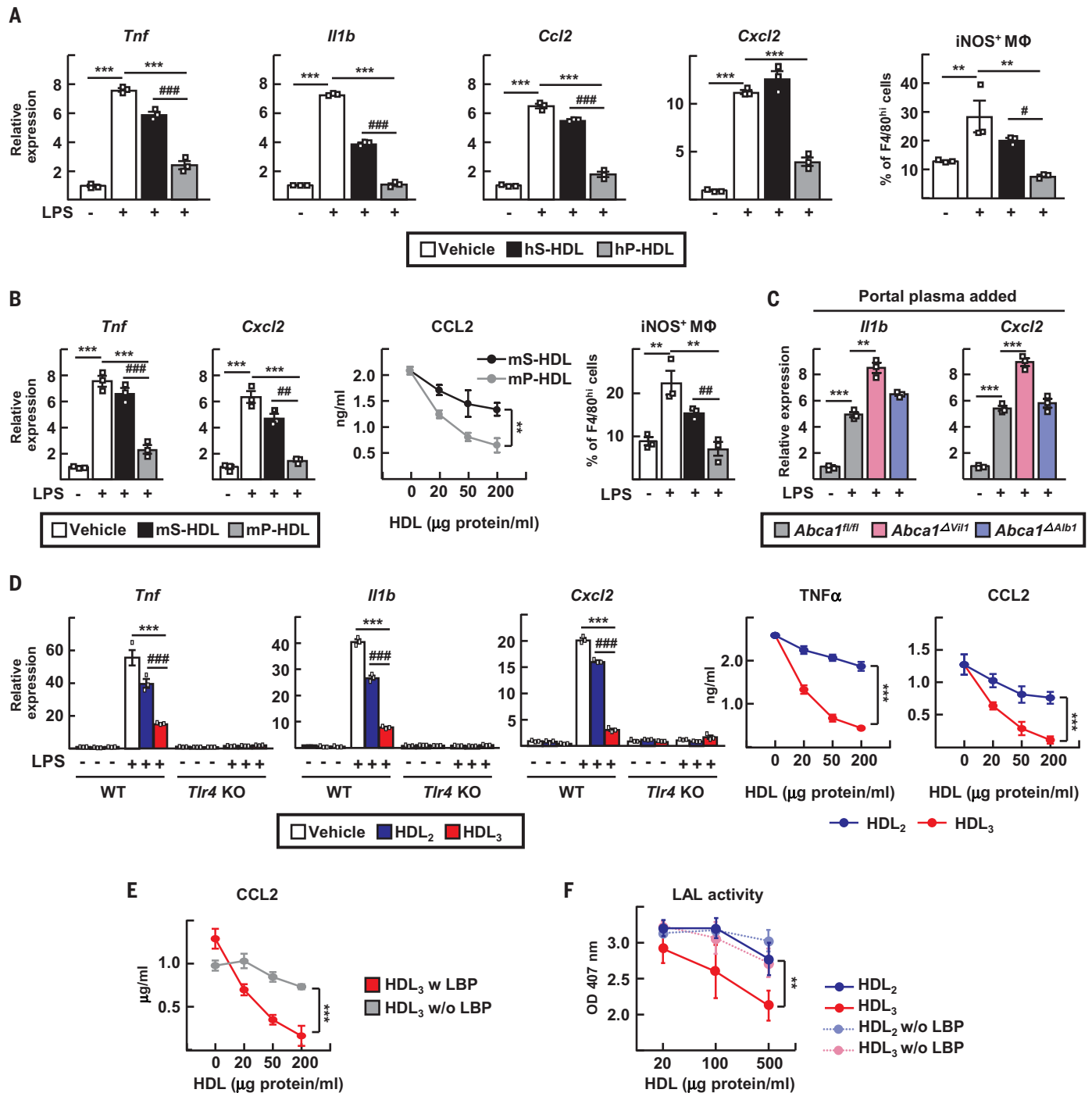
Fig. 3. Portal blood HDL₃ strongly inhibits LPS activation of KCs in an LBP-dependent manner. (**A** and **B**) LPS-treated KCs were incubated with 100 μg/ml of HDL from human (hS-HDL) or mouse (mS-HDL) systemic plasma or with human (hP-HDL) or mouse (mP-HDL) portal plasma. Analysis included RT-PCR for inflammatory mediators, flow cytometry phenotyping (iNOS⁺ F4/80hi macrophages), and CCL2 ELISA. (**C**) RT-PCR from LPS-treated KCs incubated with 5% portal vein–derived plasma from *Abca1*fl/fl, *Abca1*ΔVil1, and *Abca1*ΔAlb1 mice. (**D**) WT and TLR4⁻/⁻ KCs were incubated in LBP-containing medium with or without 20 ng/ml of LPS and 100 μg/ml of HDL₂, HDL₃, or vehicle control before RT-PCR or ELISA to detect the depicted mediators. (**E**) LPS-treated KCs were incubated with 100 μg/ml of HDL₃ with or without 1 μg/ml of LBP before CCL2 ELISA. (**F**) Endotoxin

LAL activity after 0.5 Ehrlich units (EU)/ml of *E. coli* LPS were preincubated with HDL with or without 1 μg/ml of LBP. HDL fractions in the experiments in this figure were isolated by density ultracentrifugation. Plots show mean ± SEM. Each symbol represents independent preparations of KCs from different mice. For (A) and (B), *n* = 3 different KC preparations (three experiments). For (C), *n* = 9 different KC preparations, with *n* = 3 per genotype (three experiments). In (D) and (E), *n* = 6 KC preparations (*n* = 3 each WT or TLR4 knockout). In (F), there were three independent technical replicates (three experiments) per condition per time point. **$P < 0.01$, ***$P < 0.001$, #$P < 0.05$, ##$P < 0.01$, ###$P < 0.001$. Statistical analysis on data presented as bar graphs used one-way ANOVA; data presented as concentration curves were analyzed using two-way ANOVA.
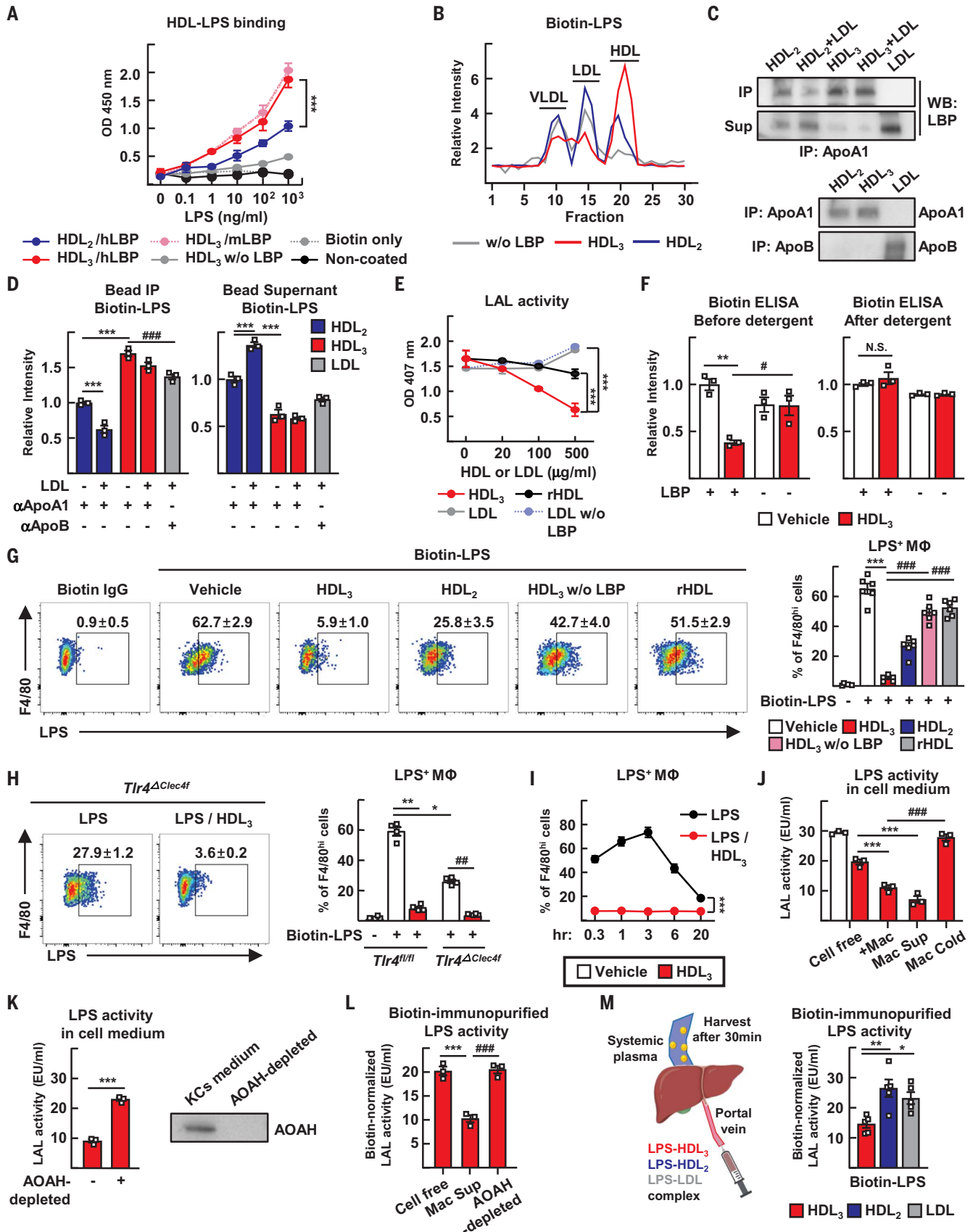
Fig. 4. HDL₃ binds LPS and masks its capacity to bind to TLR4⁺ KCs while allowing enzymatic inactivation by AOAH. (**A**) ELISA to assess HDL and biotin-LPS binding with or without LBP added. (**B**) HDL₃ or HDL₂ preincubated with biotin-LPS and incubated for 2 hours with LDL or VLDL. Biotin-LPS was then

detected in the various lipoproteins separated by FPLC. (**C** and **D**) Lipoproteins incubated with LBP and biotin-LPS for 2 hours and then retrieved using apoA1 or apoB IP. The amounts of LBP protein (C) and biotin-LPS (D) in resulting pellets (IP) versus supernatants (Sup) were measured. (**E**) Endotoxin LAL activity assessed after 0.5 EU/ml of *E. coli* LPS preincubated with different concentrations of HDL$_3$, rHDL, or LDL with or without 1 μg/ml LBP. (**F**) Biotin-LPS incubated with HDL$_3$ with or without LBP. The complex was then disrupted with SDS, and biotin-LPS was measured by streptavidin ELISA. (**G**) KCs cultured with HDL$_3$, HDL$_2$, or rHDL with or without LBP in the presence of biotinylated LPS for 3 hours, followed by streptavidin detection. Flow cytometry plots (left) and quantification (right) of binding to KCs are shown. (**H**) Binding of LPS to *Tlr4*$^{fl/fl}$ and *Tlr4*$^{\triangle Clec4f}$ KCs cultured with biotin-LPS (white) or biotin-LPS/HDL$_3$ (red). (**I**) Time course of KC binding to biotin-LPS. (**J**) LPS and HDL$_3$ (20 μg/ml) coincubated for 3 hours in cell-free medium, with KCs (+Mac), in medium conditioned by KCs (Mac Sup), or with KCs held at 4°C (Mac Cold). LAL activity was then assessed. (**K**) Endotoxin LAL activity assessed after LPS and HDL$_3$ were incubated in KC-conditioned medium from which

AOAH was depleted or not. (**L**) Biotin-LPS and HDL$_3$ incubated in the indicated medium. LAL activity was assessed, and SDS denaturation was conducted to allow for total biotin measurements. Relative LAL activity shown is normalized to a constant amount of biotin. (**M**) HDL$_3$, HDL$_2$, or LDL complexed with biotin-LPS and injected into the portal vein. Systemic plasma was harvested after 30 min. Endotoxin LAL activity and the amount of biotin were measured and normalized as in (L). All HDL fractions studied in this figure were isolated by density ultracentrifugation and, unless indicated [as in (B) to (G)], coincubated with 1 μg/ml of LBP during the assays (H to M). (A) to (F) depict three independent technical replicates (three experiments) per condition or time point. (G) to (L) used two to six different primary KC cultures (each prepared from different mice), with each symbol depicting data arising from one of the KC cultures. (M) is from one experiment using 15 WT mice (*n* = 5 mice per condition). *$P < 0.05$, **$P < 0.01$, ***$P < 0.001$, #$P < 0.05$, ##$P < 0.01$, ###$P < 0.001$. Statistical analysis on data presented as bar graphs used one-way ANOVA except for (K), for which a *t* test was used; data presented as concentration curves were analyzed using two-way ANOVA.

and S100A9$^+$) into the liver (Fig. 5D). LPS bioactivity in the portal vein was elevated by small bowel resection (Fig. 5E) and was associated with increased intestinal permeability (Fig. 5F), reductions in the epithelial junction proteins ZO-1 and occludin (*Ocln*) (Fig. 5G), and elevated plasmalemma vesicle-associated protein 1 (PV1) in villus capillaries (Fig. 5H) draining into the portal vein (*29*).

Reduced liver fibrosis and inflammatory changes characterized KC-specific *Clec4f*-Cre×*Tlr4*$^{flox/flox}$ male mice compared with littermate controls (*30*) (Fig. 5, I to M). Female mice (fig. S5) developed disease similarly to males. Bone marrow transplants in which mice received *Tlr4*$^{-/-}$ bone marrow confirmed the role of TLR4 (fig. S6). Thus, TLR4 expressed by KCs participates critically in liver fibrosis after small bowel resection.

Disruption of enterically derived HDL exacerbates liver injury

Portal venous HDL-C decreased after small bowel resection (Fig. 6A), possibly a consequence of the loss of bowel mass that might normally contribute to HDL biogenesis. Expression of ABCA1 sharply increased from the proximal to distal small bowel, whereas apoA1 modestly rose, overall fitting with the ileum as the main site for HDL production in the small bowel (Fig. 6B). When we modified the region of the bowel resected to remove the proximal 50% or distal 50% portion of the small intestine, HDL-C in portal blood decreased more substantially after distal resection (Fig. 6C). Accordingly, liver injury and inflammatory markers were greater in response to distal resection (Fig. 6D and fig. S7, A and B).

We compared liver injury outcomes in *Abca1*$^{\triangle Vil1}$ mice versus control *Abca1*$^{fl/fl}$ mice or *Abca1*$^{\triangle Alb1}$ mice after small bowel resection. HDL-C in portal blood was further reduced in *Abca1*$^{\triangle Vil1}$ mice (Fig. 6E), and these mice indeed exhibited greater liver injury, fibrosis, and inflammation (Fig. 6, F to I). Sham

surgery did not provoke liver injury (fig. S7, C to F). After small bowel resection, LPS bioactivity was elevated in *Abca1*$^{\triangle Vil1}$ mice (Fig. 6J, upper bar graph). However, the absolute amount of LPS in portal plasma matched that of other groups (Fig. 6J, lower bar graph), suggesting that the lower HDL-C in *Abca1*$^{\triangle Vil1}$ mice led to increased LPS activity for a given quantity of LPS because of reduced neutralization.

Liver inflammation was elevated in *Abca1*$^{\triangle Vil1}$ mice over control mice after perturbations including 12 weeks of high-fat diet (HFD) feeding or 4 weeks of the Lieber–DiCarli alcohol diet (ALD) (Fig. 6, K to M). These additional liver injury models are associated with elevated LPS translocation across the intestinal barrier (*31*, *32*), elevations that we verified and that were in keeping with reduced HDL-C in the portal vein and apparent increased fat storage in the liver of the HFD model (fig. S7, G to I). Thus, enterically derived HDL protects against injury in multiple mouse models of liver damage.

Activation of LXR in the intestine increases HDL output and protects against liver injury

Liver X receptors (LXRs) are transcription factors that govern the expression of HDL-related genes such as *Abca1*. Low-dose LXR agonists such as GW3965, when administered orally, bypass activation of LXRs in the liver while targeting the intestine (*33*, *34*). We thus administered GW3965 orally at a low dose in mice subjected to 75% small bowel resection and followed gene expression in the ileum and liver (Fig. 7, A to E, and fig. S8). GW3965 treatment prompted increases in *Abca1* and *Apoa1* mRNA in the ileum (Fig. 7, A and C). The impact of low-dose oral GW3965 on these genes and on LXR target genes associated with de novo lipogenesis was minimal in the liver (Fig. 7, B and D). However, inflammatory and collagen-remodeling genes in the liver were markedly down-regulated in response to GW3965 in *Abca1*$^{fl/fl}$ mice that retained expression of in-

testinal HDL (Fig. 7E and fig. S9). These genes remained elevated in *Abca1*$^{\triangle Vil1}$ mice (Fig. 7E), confirming that the effect of GW3965 depended on intestinal HDL. Oral, low-dose GW3965 did not affect *Abca1* or related genes in peritoneal macrophages adjacent to the portal venous drainage in the mesentery (fig. S8A). Some intestinal macrophages were positive for ABCA1 (fig. S8B), but deletion of ABCA1 in macrophages neither affected gene expression in the ileum nor altered portal HDL-C (fig. S8C). No changes to the liver were apparent in *Abca1*$^{\triangle Vil1}$ mice compared with littermate *Abca1*$^{fl/fl}$ controls receiving sham operations (fig. S10).

Functionally, portal venous HDL-C, remaining predominantly in the form of HDL$_3$, was increased by GW3965 in *Abca1*$^{fl/fl}$ mice but not in *Abca1*$^{\triangle Vil1}$ mice (Fig. 7, F and G). Indeed, oral GW3965 prominently reduced fibrosis and inflammation in the liver after small bowel resection (Fig. 7, H to K) but was unable to do so in *Abca1*$^{\triangle Vil1}$ mice (Fig. 7, H to K). Thus, orally delivered low-dose GW3965 protects the liver from inflammation and fibrosis in a manner that depends upon its capacity to increase enteric HDL.

Discussion

Intestinal epithelial cells produce HDL particles (*11*), but neither the fate nor the function of intestinal HDL has been clear. We show here that the intestine produces the small form of HDL called HDL$_3$ and that it is enriched in LBP. This HDL is shuttled to the liver through the portal vein. By the time it reaches the portal blood, it is already complexed with LBP, and the LPS that it carries is masked so that it does not bind to liver KCs, circumventing the induction of proinflammatory and profibrotic genes. The intestinal epithelial location for HDL production allows the local capture of LPS before it gains access to downstream tissue.

That HDL may prevent LPS from binding to cells in the liver has been noted earlier by
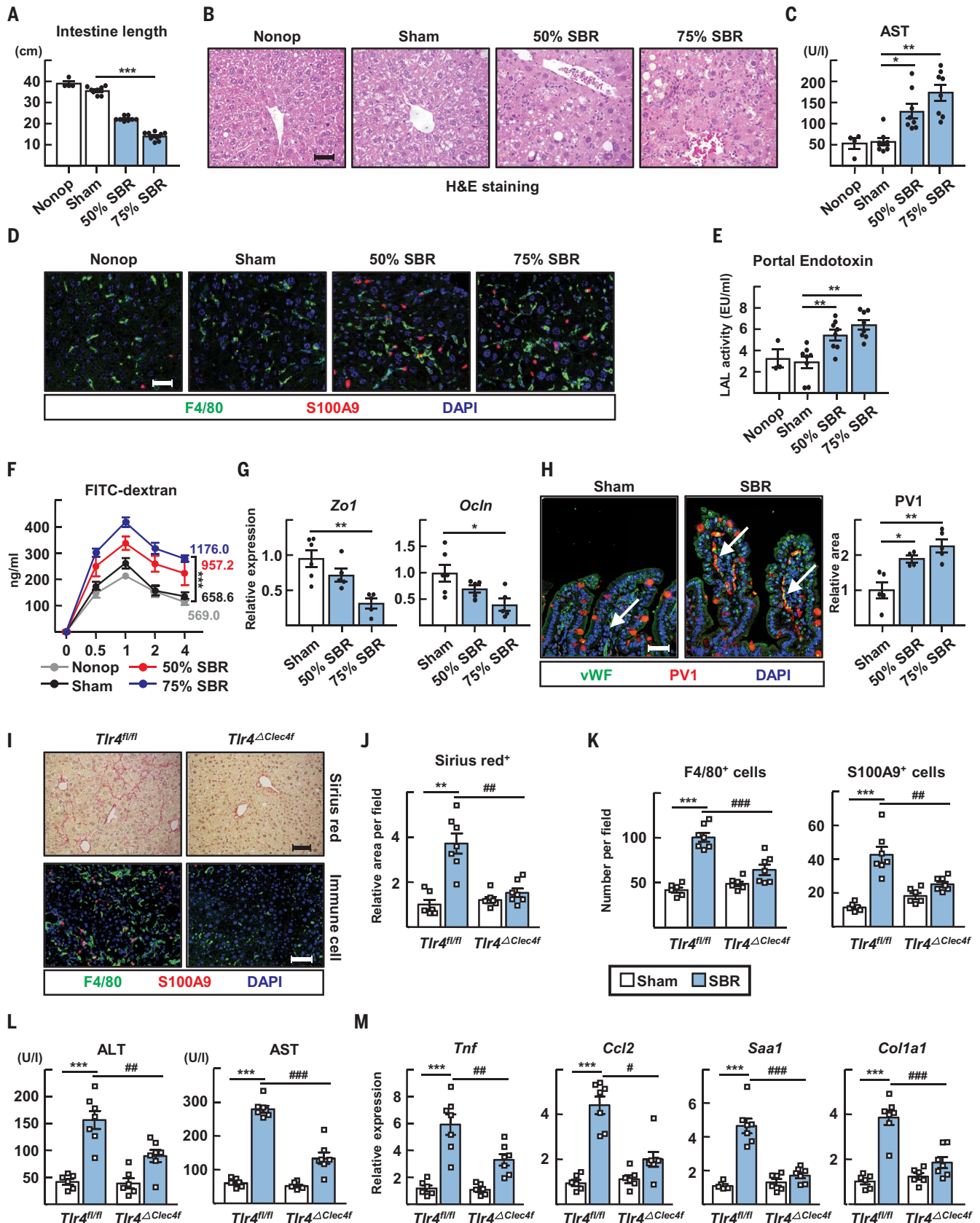
Fig. 5. Small bowel resection triggers TLR4-mediated liver inflammation.
(**A** to **H**) Small bowel resection (SBR) operations were conducted on WT
mice. Nonoperated (Nonop) (*n* = 4), sham (*n* = 8), 50% SBR (*n* = 8), and

75% SBR (*n* = 8) mice were euthanized 12 weeks later. (A) Total length
of the remaining small intestine. (B) Representative hematoxylin and eosin
(H&E)–stained liver sections. Scale bar, 50 μm. (C) Plasma AST levels.

(D) F4/80$^+$ macrophages and S100A9$^+$ neutrophils in liver sections. Scale bar, 50 μm. (E) LAL endotoxin activity in portal plasma. (F) Kinetics of FITC-dextran translocation from intestine to peripheral blood. Area under the curve was measured. (G) qRT-PCR for intestinal mRNA transcripts encoding tight junction proteins. (H) Staining for von Willebrand Factor (vWF) (blood vessel) and PV1 in intestinal sections (left). Note that goblet cell mucin stains with the PV1 antibody, possibly nonspecifically. Relative increase in PV1 staining of vWF$^+$ vessels (highlighted by white arrows) after SBR (right). Scale bar, 50 μm. (I to M) Sham or 75% SBR operations were performed on Tlr4$^{fl/fl}$ and Tlr4$^{\triangle Clec4f}$ male mice, which were euthanized after 10 weeks. (I) Sirius red and immunostaining of liver sections. Scale bars, 100 μm. (J) Relative sirius red–positive area per field. (K) Numbers of F4/80$^+$ macrophages and S100A9$^+$ neutrophils per field. (L) Plasma ALT and AST levels. (M) Hepatic mRNA transcripts of inflammatory genes analyzed by qRT-PCR. (A) to (G) are the results of analysis of 30 WT mice combined from two experiments, with n = 4 to 10 mice per condition (nonoperated, sham, 50% SBR, or 75% SBR). (I) to (M) depict one experiment arising from analysis of 26 mice (n = 6 to 7 per genotype with or without SBR). Each symbol represents data from an individual mouse. *P < 0.05, **P < 0.01, ***P < 0.001, #P < 0.05, ##P < 0.01, ###P < 0.001. Statistical analysis on data presented as bar graphs used one-way ANOVA; data presented as concentration curves were analyzed using two-way ANOVA.

Munford and colleagues (35), who pioneered our understanding of the role of AOAH in inactivating LPS (26). Indeed, we show that whereas LBP-containing HDL$_3$ suppresses recognition of LPS by KCs, it remains accessible to AOAH inactivation. It is unknown how HDL$_3$ prevents TLR4 recognition of LPS but not that of AOAH. The difference may relate to the role of LBP. Because TLR4 depends upon LBP shuttling to CD14 to interact with LPS, the HDL$_3$–LBP complex may most effectively mask this interaction by masking the critical epitope that would support LBP-mediated handoff of LPS to CD14. However, AOAH activity does not require LBP or CD14 and thus may recognize LPS in the HDL$_3$ particle through a region of LPS not masked by LBP.

HDL suppressed the LPS-mediated activation of KC, as well as the proinflammatory action of mediators such as lipoteichoic acid, which also interacts with HDL through LBP (36). Enterically derived HDL may bind and neutralize other microbial cargo not yet identified. Furthermore, the absence of HDL-mediated neutralization of microbial lipids such as LPS may affect the course of inflammation in locations other than the liver. For example, in Crohn's disease, a major inflammatory bowel disease, apoA1 is the most substantially down-regulated gene in the affected ileal tissue (37). In cardiovascular disease and sepsis, HDL$_3$ rather than HDL$_2$ levels correlate with better health outcomes (38, 39). The connection between disease pathogenesis in these various conditions and enteric HDL is ripe for future investigations.

Unanswered questions arise from this study. First, how do LPS and LBP interact with HDL$_3$ in a manner that masks the bioactivity of LPS? Although LBP is a critical promoter of TLR4 signaling, it conversely mediates suppressed signaling in the presence of HDL$_3$. The structural basis of this unexpected result deserves future attention. Moreover, studies in whole-body knockout mice likely obscure the anti-inflammatory contribution of LBP when bound to HDL$_3$ because of its other well-characterized proinflammatory role. Finally, are other components of HDL$_3$ needed to support the LPS-masking action of HDL$_3$ that we identify here?

Yet another mystery is why most portal venous HDL-C derives from the intestine. We had expected that portal venous blood HDL would arise from both portal and systemic sources. However, although systemic HDL clearly arrived to the gut or mesentery, as evidenced by efficient entry into intestine-draining mesenteric lymphatics, it was not strongly detected in the portal vein. These data suggest the existence of unknown trafficking steps, including the possible extravasation of systemic HDL near or within the intestine. After extravasation, HDL$_2$ that has entered or formed in the intestinal interstitium from the periphery may be too large to enter the fenestrated blood vessels that drain to the portal blood such that only enterically derived HDL$_3$ gains efficient access. Consistent with this possibility, mesenteric lymph is relatively deficient in the smaller HDL$_3$ particles but relatively enriched in HDL$_2$ (40). In contrast to our findings and those of others (12), studies in rats have found that the intestine routes HDL to lymph (41, 42). Although this discrepancy may be a species difference, studies in humans are more consistent with our present findings (43, 44) than with those in the rat. Moreover, it has been proposed that the use of lecithin-cholesterol acyltransferase inhibitors in these rat studies aberrantly affected the results (12).

We believe that this research has strong translational potential. In humans, like mice, portal blood was enriched in HDL$_3$ and potently suppressed KC activation in response to LPS. We used three murine models of liver injury involving nutritional, alcoholic, or surgical insult to the intestine. All showed that intestinally derived HDL reduced liver injury. From a therapeutic perspective, oral delivery of LXR agonists proved effective in protecting the liver by upregulating HDL within the intestine, consistent with another recent study that engineered mice so that LXR activity was genetically augmented selectively in the intestine (45). Furthermore, our profiling and functional analysis revealed that the intestinal epithelium must express ABCA1, which is critical for HDL biogenesis, in order for a low-dose, oral LXR agonist to protect the liver. LXR agonists have failed to find utility in the clinical setting to date, but orally restricted LXR agonists remain promising (46, 47). Our findings highlight the possibility that enteric HDL–raising LXR agonists have appeal for the treatment of various forms of liver injury. However, if suitable LXR agonists cannot be developed for application in humans, then other approaches to elevating intestinal HDL should be explored.

MATERIALS AND METHODS

Mice

C57BL/6 WT, Tlr4$^{-/-}$ (B6.B10ScN-Tlr4$^{lps-del}$/JthJ; JAX #007227), Vil1-Cre (B6.Cg-Tg(Vil1-cre)997Gum/J; JAX #004586), Alb1-Cre (B6.FVB(129)-Tg(Alb1-cre)1Dlr/J; JAX #016832), Abca1$^{fl/fl}$ (B6.129S6-Abca1^{tm1Jp}/J; JAX #028266), Tlr$^{fl/fl}$ (B6(Cg)-Tlr4$^{tm1.1Karp}$/J; JAX #024872) Clec4f-Cre (C57BL/6J-Clec4f$^{em1(cre)Glass}$/J; JAX #033296), Abca1/g1$^{fl/fl}$ (B6.Cg-Abca1^{tm1Jp} Abcg1^{tm1Tall}/J; JAX #021067), and Lyz2-Cre (B6.129P2-Lyz2$^{tm1(cre)Ifo}$/J; JAX #004781) mice (7–10 weeks of age) were originally purchased from Jackson Laboratories and housed in a specific-pathogen-free room at 22 to 24°C and 50 to 60% humidity with a 12-hour light-dark cycle. We previously generated and described PGA$^{KI/+}$ mice (15). Lyz2-Cre×Abca1/g1$^{fl/fl}$ breeders were provided by Dr. R. Apte and Cd36-knockout mice (both strains also on C57BL/6 background) by Dr. N. Abumrad at Washington University. All experiments were performed in a blinded and randomized fashion. Mice were housed on a 12-hour light-dark cycle in a temperature-controlled, specific-pathogen-free unit with food and water provided ad libitum. The studies were approved by the Washington University Animal Studies Committee (protocols 20170154, 20170252, and 20-0032) or the Medical College of Wisconsin Animal Studies Committee (protocol AUA00004173) in accordance with the National Institutes of Health laboratory animal care and use guidelines.

Small bowel surgery and associated treatments or transplants

For small bowel resection experiments, mice underwent a 50% proximal (jejunal) bowel resection, 75% proximal bowel resection, or
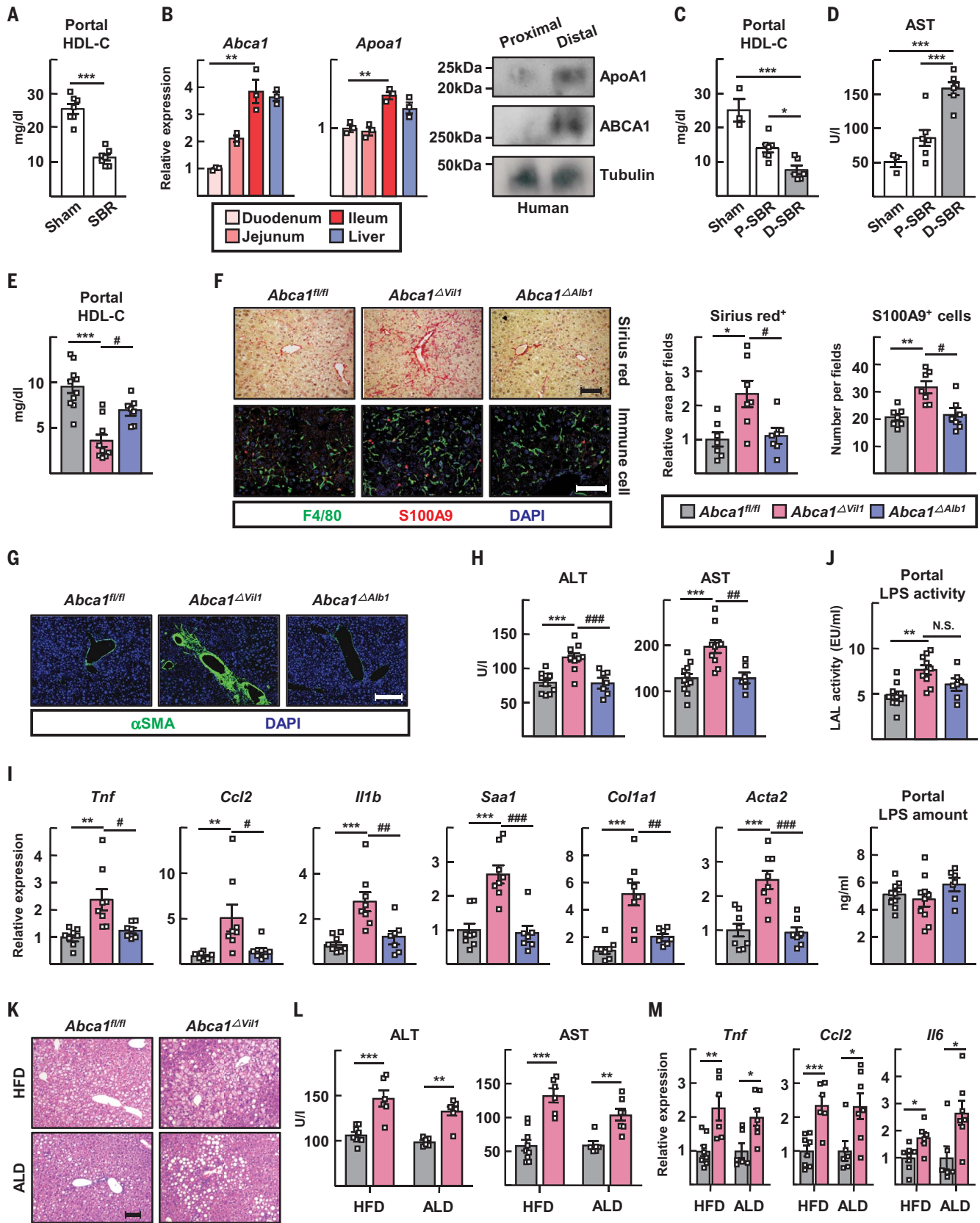
Fig. 6. Disruption of enteric HDL production worsens small bowel resection–induced liver injuries. (**A**) Portal HDL cholesterol levels in mice receiving sham or 75% SBR operations. (**B**) RT-PCR for *Abca1* and *Apoa1* in mouse duodenum, jejunum, ileum, and liver (left). Protein expression of apoA1 and ABCA1 in human proximal and distal gut were analyzed by immunoblotting (right). (**C** and **D**) SBR operations were conducted for WT mice. Mice receiving

sham (n = 3), proximal 50% SBR (P-SBR) (n = 7), and distal 50% SBR (D-SBR) (n = 6) operations were euthanized 10 weeks later. (C) Portal HDL cholesterol levels. (D) Plasma AST levels. (**E** to **J**) 75% SBR operations were performed for *Abca1*^fl/fl (n = 10), *Abca1*^ΔVil1 (n = 10), and *Abca1*^ΔAlb1 (n = 7) mice, which were euthanized 8 weeks later. (E) Portal HDL cholesterol levels. (F) Representative sirius red staining of liver sections (left, top row) and relative area per field (near right). F4/80^+ macrophages and S100A9^+ neutrophils were visualized (left, bottom row); cell numbers per field are shown (far right). Scale bars, 100 μm. (G) Representative anti-SMA immunostaining of liver sections. Scale bar, 200 μm. (H) Plasma ALT and AST levels. (I) Hepatic RT-PCR for inflammatory genes. (J) Portal LAL LPS activity (top) and LPS quantification by ELISA (bottom). (**K** to **M**) *Abca1*^fl/fl and *Abca1*^ΔVil1 male mice were fed HFD or ALD. (K) Representative H&E–stained liver sections. Scale bar, 100 μm. (L) Plasma ALT and AST levels. (M) RT-PCR for inflammatory genes. (A) to (C) show results from n = 3 to 7 mice per condition using WT mice (one experiment each panel). (E) to (I) combine data from two experiments using 28 mice (n = 7 to 11 mice per genotype). (L) and (M) depict two experiments (one HFD, one ALD) from n = 15 mice on HFD (n = 9 *Abca1*^fl/fl mice, 6 *Abca1*^ΔVil1 mice) or n = 13 mice on ALD (n = 6 *Abca1*^fl/fl mice, 7 *Abca1*^ΔVil1 mice). *P < 0.05, **P < 0.01, ***P < 0.001, #P < 0.05, ##P < 0.01, ###P < 0.001. Statistical analysis on data presented as bar graphs used one-way ANOVA except for (A), for which a t test was used.

sham control operation (bowel transection with reanastomosis alone), as previously described (*28*). In brief, through a midline laparotomy, the small bowel was exteriorized and transected 1–2 cm distal from the ligament of Treitz and ~12 cm (for 50% resection) or 6 cm (for 75% resection) proximal to the ileocecal junction. For sham operations, a transection 12 cm proximal to the ileocecal junction with immediate reanastomosis was performed. For distal 50% small bowel resection, the ileum (last 12 cm of small bowel) was removed with an anastamosis of the jejunum to a small cuff of small bowel on the cecum. All anastomoses were hand sewn end to end with interrupted 9-0 nylon sutures. Postoperative care included housing in an incubator for temperature stability and 24 hour fasting before starting a liquid diet (PMI Micro-Stabilized Rodent Liquid Diet LD 101; TestDiet), on which the mice were maintained for 8–12 weeks until euthanasia.

For bone marrow transplants, WT recipient mice received whole-body irradiation at a dose of 11 Gy at 8 weeks of age, and then were intravenously injected with 5 × 10^6 bone marrow cells from WT or *Tlr4*^−/− donor mice. After 4 weeks, short bowel resections were conducted.

For LXR agonist treatment, GW3965 (Sigma-Aldrich, #G6295) was suspended in 0.5% carboxymethyl cellulose and orally administered twice weekly at 1 mg/kg body weight per day for the last 5 weeks in the 10-week period after intestinal resection. The different experimental groups of mice maintained a similar body weight during liquid diet feeding and/or drug treatment.

Dietary challenge models

Where specified, mice were given HFD or ALD to induce liver inflammation and injury (*48*, *49*). The HFD study, containing 60% kcal from fat (Research Diets, #D12492), was conducted for 12 weeks. For ethanol feeding, the mice were acclimated to increasing alcohol concentration of 2.1, 4.2, and 6.4% v/v (ethanol and liquid diet) over 3 days, respectively. After alcohol adaptation, a 6.4% ethanol–enriched diet was supplied in the same liquid diet used after small bowel resection surgeries (diet changed daily) for 4 weeks. In supplemental experiments, mice were fasted (with ad libitum access to water) for up to 20 hours, or challenged for 3 weeks with an atherogenic diet containing 42% kcal from fat (Harlan Teklad, #TD.88137).

Immunostaining and confocal microscopy

Left lobes of liver tissues and small intestines were excised and fixed in 4% paraformaldehyde (Santa Cruz Biotechnology) overnight at 4°C. Ten-micrometer paraffin-embedded sections were prepared and slides were boiled in Diva Decloaker solution (Biocare Medical, #DV2004) in a pressurized chamber for 15 min. Sections were blocked in phosphate-buffered saline (PBS) containing 5% donkey serum, 1% bovine serum albumin (BSA) (Sigma-Aldrich), and 0.03% Triton X-100 (Plusone, #17-1315-01) for 1 hour, then incubated with rat anti-F4/80 (Abcam, #ab6640), goat anti-S100A9 (R&D Systems, #AF2065), rabbit anti-von Willebrand Factor (DAKO, #a0082), rat anti-PV1 (BD pharmingen, #550563), or rabbit anti-ABCA1 (Novus Biologicals, NB400-105) at 4°C overnight. Primary antibodies were detected using Cy3- or Cy5-conjugated secondary antibodies (Jackson ImmunoResearch). The stained sections were imaged using an SP8 confocal microscope (Leica) equipped with nine lasers and four tunable detectors (two hybrid, two tunable) and a 20× HC PL Apo CS 2 multi-immersion objective, numerical aperture 0.75. Images were processed with Imaris software (Bitplane). Ten fields were quantified and averaged for each sample, with cell counts per image quantified using Image J software (NIH). All slides were analyzed in a blinded and randomized fashion.

Quantitative real-time polymerase chain reaction (qRT-PCR)

Total RNA from tissues or cells was isolated by using RNeasy Mini or Micro kits according to the manufacturer's protocol (Qiagen). cDNA was synthesized using the high-capacity cDNA reverse transcription kit (Applied Biosystems, #4368814). qRT-PCR experiments were performed using ABI StepOnePlus Real-Time PCR machine with specific primers (Applied Biosystems). Primer sequences are available upon request. The relative transcriptional expression of target genes was evaluated by the Eq. $2^{-\Delta Ct}$ (ΔCt = Ct of target gene minus Ct of 18S rRNA). Relative transcription, where plotted, was calculated with the mean of the control group set as 1.

Intestinal permeability assay

After the mice had fasted for 4 hours, 200 mg/kg body weight of 4-kDa fluorescein isothiocyanate (FITC)–dextran (Sigma-Aldrich) was administered by gavage. After 0.5, 1, 2, or 4 hours, blood for the preparation of plasma was collected from the tail vein, and the fluorescence intensity of the samples and standards was read at excitation 485 nm/emission 525 nm using the Cytation 5 Cell Imaging Multi-Mode Reader (BioTek).

Photoactivation of PGA1^KI/+ mice

For phototagging HDL from skin, 8- to 10-week-old PGA1^KI/+ mice were anesthetized and a region of shaved skin was photoconverted using a SOKY, Violet 405 nm 500 mW (FDA), PL-405-500B laser, as described previously (*15*). For photoactivation of the lumen of the small intestine of anesthetized mice, we stretched the mesentery and intestine over the solid surface of a Petri dish, located the region of interest, and surgically clipped the bowel just enough so that we could thread into the lumen a fiber-optic endoscopic laser (Laserland, Violet 405 nm 100 mW) to photoactivate enterocytes. Unless otherwise specified, three areas were activated for one data point, with the laser being held on for 10 s and off for 20 s, cycling for 1 min 10 s to achieve three exposures per location. For photoactivation of the exterior of the small intestine, the Laserland Violet 405 nm 100 mW 5V laser was used to activate area of 14.668 mm^2 of gut with a similar on–off cycle as for the intestinal lumen.

Collection of blood and lymph

The portal blood was collected using a 33-gauge needle to a volume of 40 μl per mouse. Systemic blood was collected from the inferior vena cava using a 26-gauge needle in EDTA-containing tubes. Mesenteric lymph fluid was also collected, and the fluorescence intensity of plasma or lymph fluid was measured using the Cytation 5 Cell Imaging Multi-Mode Reader (BioTek). Mesenteric lymphatic cannulations were accomplished under general anesthesia using an
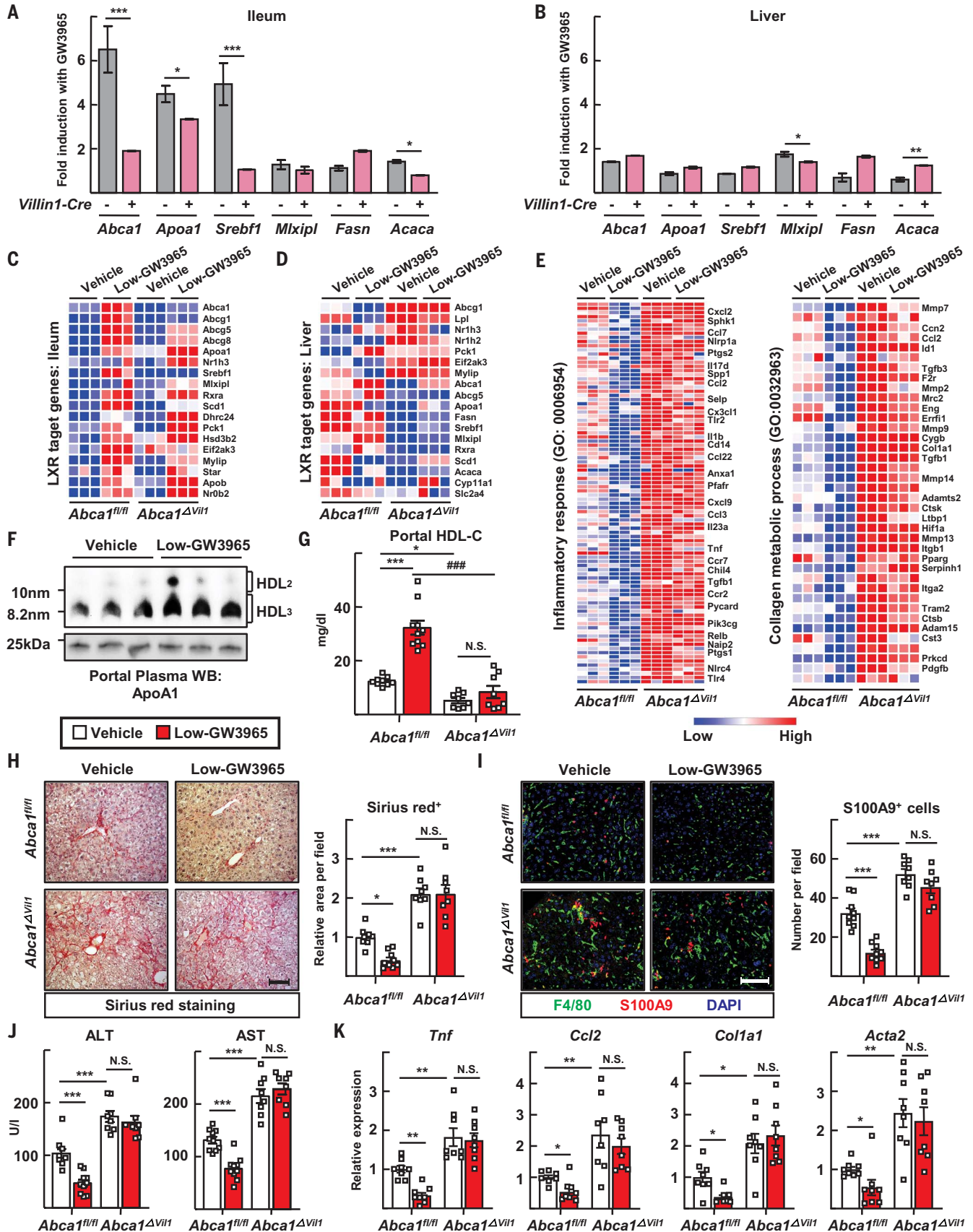
Fig. 7. Intestine-restricted activation of LXR ameliorates liver injury in a manner dependent upon enteric HDL production. (**A** to **E**) $Abca1^{fl/fl}$ and $Abca1^{\Delta Vil1}$ mice received vehicle ($n = 10$ $Abca1^{fl/fl}$ mice, $n = 8$ $Abca1^{\Delta Vil1}$ mice) or 1 mg/kg/day GW3965 ($n = 10$ $Abca1^{fl/fl}$ mice, 8 $Abca1^{\Delta Vil1}$ mice) by gavage twice weekly in the last 5 weeks of a 10-week feeding after SBR (Low-GW3965). (A and B) RT-PCR analysis of select target genes in the ileum and liver tissues was used to determine fold induction in response to GW3965 treatment. (C and D) Heatmap of mRNA transcripts of LXR-regulated genes in the ileum and liver tissues. (E) Heatmap of mRNA transcripts encoding genes associated with the inflammatory response or collagen metabolism within the liver according to GW3965 treatment and genotype. (**F**) Immunoblots for apoA1 to detect HDL after portal vein plasma were run on a nondenaturing gel. (**G**) Portal plasma HDL cholesterol levels. (**H**) Sirius red staining of liver sections (left) and relative area per field (right). Scale bar, 100 μm. (**I**) F4/80⁺ macrophages and S100A9⁺ neutrophils visualized by immunofluorescence in liver sections (left) (scale bar, 100 μm) and cell numbers per field counted (right). (**J**) Plasma ALT and AST levels. (**K**) RT-PCR measuring inflammation- or fibrosis-associated mediators. Plots show mean ± SEM in male mice, with each symbol on the bar graphs representing a single mouse with data combined from two experiments; $*P < 0.05$, $**P < 0.01$, $***P < 0.001$, $\#\#\#P < 0.001$. t tests were used for statistical comparisons in (A) and (B); one-way ANOVA was used for statistical comparisons in (G) to (K).

operating microscope. A midline laparotomy with an extension to a left subcostal incision was made and the intestine was mobilized to expose the mesenteric lymphatic duct proximal to the cisterna chyli. A small incision was made on the mesenteric lymphatic duct and gently cannulated using polyethylene tubing (inner diameter, 0.28 mm; outer diameter, 0.61 mm; Intramedic, Sparks, MD). At the completion of the collection, the mouse was euthanized.

Preparation of HDL fractions

Human and mouse plasma collected from the portal vein or peripheral vein (inferior vena cava for mouse, antecubital vein for human) was collected and ultracentrifuged overnight using standard methodology at 100,000g at 4°C in sequential steps, adjusting the solution to 1.063 g/ml using KBr (Sigma-Aldrich, #221864) to remove LDL. Then the HDL fraction was prepared by another centrifugation at 100,000g after further adjusting density of the solution to 1.21 g/ml with KBr. Isolated HDL fractions were dialyzed using the Slide-A-Lyzer Dialysis cassette kit (Thermo Fisher Scientific) with PBS solutions containing NaCl, Tris, and EDTA for 4 hours at 4°C to remove KBr. Human HDL₂ (1.063-1.125 g/ml) and HDL₃ (1.125-1.21 g/ml) fractions were obtained from GenWay Biotech.

FPLC and measurement of HDL cholesterol

Fifty microliters of blood from mice fasted for 4 hours was collected in microcentrifuge tubes containing 10 μl of 0.5 mM EDTA and then centrifuged at 500g to collect plasma. For cholesterol distribution of total lipoproteins, plasma was prepared and 100–200 μl was flowed over a Superose 6 10/300GL gel filtration column (GE Healthcare) to separate the different classes of lipoproteins. Cholesterol in each fraction was measured by an enzymatic assay kit (Wako Diagnostics Cholesterol E, #439-17501). An HDL cholesterol assay kit (Cell Biolabs, #STA-394) was used to measure HDL-C levels.

Immunoblots

Protein immunoblotting was performed using rabbit anti-mouse apoA1 (Meridian Life Sciences), rabbit anti-human apoA1 (Millipore,

#MAB011), rabbit anti-human ABCA1 (Novus Biologicals, #NB400-105), mouse anti-PON1 (Abcam, #ab24261), rabbit anti-ApoB (Proteintech, #20578-1), rabbit anti-LBP (Abcam, #ab233524), rabbit anti-AOAH (Proteintech, #12911-1), rabbit anti-SERPINA1 (Thermo Fisher Scientific, #PA5-16661), mouse anti-ApoE (kindly provided by D. M. Holtzmann, Washington University), or rabbit anti-albumin (Proteintech, #16475-1) antibodies. Table S2 specifies the dilutions of the antibodies used. The HDL fractions were loaded to achieve the same protein concentration per lane, and plasma was loaded without dilution. For native gels, the samples were diluted in 2× native sample buffer (Bio-Rad) and run on 4 to 20% Mini-PROTEAN Tris-glycine gels (Bio-Rad) with Tris-glycine running buffer. For denaturing gels, the samples were diluted in 2× Tris-Glycine-SDS sample buffer (EZ Bioresearch) and heated at 95°C for 10 min. The samples were loaded onto 4 to 20% Mini-PROTEAN gels and run with Tris-glycine-SDS running buffer. The separated proteins were transferred to 0.45-μm polyvinylidene fluoride membrane (Milipore, #IPVH00010) with Tris-glycine transfer buffer for 2 hours at 20 V. Membranes were blocked with 5% nonfat dry skim milk (Bio-Rad, #170-6404) for 1 hour, and p rimary antibodies were incubated overnight at 4°C. After incubation with horseradish peroxidase–conjugated secondary antibodies, signal was detected using Clarity Western ECL solution (Bio-Rad).

Electron microscopy of HDL particles

The isolated HDL fractions were diluted to 15 μg/ml of total protein and negatively stained with 1% uranium acetate. The samples were deposited on carbon-coated, 200-mesh copper grids (Electron Microscopy Sciences). Images were acquired with a transmission electron microscope (TEM; JEOL, #JEM-1400^Plus) at 120 KeV and 80,000× or 150,000× magnifications. The diameter of HDL particles was measured using ImageJ software.

Isolation or culture of liver immune cells and macrophages

For quantification of neutrophils, monocyte-derived macrophages, and KCs in livers of mice subjected to short bowel resection or sham

surgery, livers were collected and homogenized in Hank's buffered saline solution containing 1.49 mg/ml of collagnase type IV (Sigma-Aldrich, #C5139) and dissociated using the gentleMACS Octo Dissociator (Miltenyi Biotec). After centrifugation at 50g, the supernatant containing nonparenchymal cells was separated using 33% Percoll (GE Healthcare).

For KC isolation and culture, the livers of 7- to 10-week-old male C57BL/6 mice were perfused through the inferior vena cava with collagenase type IV solution as described previously (50). The cell suspension was centrifuged. Cell suspensions collected in the supernatant were collected and again centrifuged in 50%/25% Percoll (GE Healthcare). The layer containing liver macrophages was plated in RPMI-1640 (Hyclone) containing 10% fetal bovine serum (FBS). After 2 hours of culture to allow for cell attachment, the cell medium was changed to "vehicle" medium, which was serum-free RPMI-1640 containing 1 μg/ml of recombinant LBP (R&D Systems, #6635-LP) for 3 hours of culture. HDL preparations were added, or not, to these cultures with 20 ng/ml of LPS (Sigma-Aldrich, #L2630), 10 μg/ml lipoteichoic acid (LTA) (Sigma-Aldrich, #L2515), 10 μg/ml CpG DNA (Invivogen, #tlrl-1826), 100 ng/ml TNF (Sigma-Aldrich, #T7539), or 100 ng/ml IL-1β (Sigma-Aldrich, #I5271).

Flow cytometry

Isolated liver immune cells and cultured liver macrophages were collected and counted in an automated cell counters (Cellometer Auto X4; Nexelcom Bioscience) after staining for acridine orange (Sigma-Aldrich). Antibodies (details in table S2) including BUV396-anti-CD45 (BD Biosciences, #563791), FITC-anti-Ly6G (BioLegend, #127605), APC/Cy7-anti-F4/80 (BioLegend, #123117), PerCP/Cy5.5-anti-Ly6C (BioLegend, #128011), PE/Cy7-anti-CD31 (BioLegend, #102417), Alexa Fluor 488-anti-iNOS (Thermo Fisher Scientific, #53-5920-82), APC-anti-CD11b (Thermo Fisher Scientific, #17-0112-82), PE-anti-Tim4 (Thermo Fisher Scientific, #12-5866-82), or goat anti-Clec4f (R&D Systems, #AF2784) were incubated with FACS buffer (2% FBS, 2 mM EDTA, and sodium azide in PBS) on ice for 30 min. In some experiments, the primary cultures of KCs were

incubated with 100 ng/ml of biotinylated LPS (Invivogen, #tlrl-lpsbiot) for 2 hours. Then, biotin was detected using PE/Cy7-streptividin (BioLegend, #405206). After surface staining of biotin, in some experiments, internalized biotin-LPS was stained using BV605-streptavidin (BioLegend, #405229) in cells permeabilized using the Intracellular Fixation & Permeabilization Buffer Set (Thermo eBioscience, #88-8824). After washing and resuspension, cells were analyzed on a BD Biosciences FACS Symphony machine and analyzed by FlowJo software (BD Biosciences).

Enzyme-Linked Immunosorbent Assay

Enzyme-linked immunosorbent assay (ELISA) kits were used according to the manufacturer's protocol and included the AST Activity Assay Kit (Sigma-Aldrich, MAK055), TNF-α (Sigma-Aldrich, RAB0477), or CCL2 ELISA (Sigma-Aldrich, #RAB0055). Limulus amebocyte lysate (LAL) endotoxin activity was measured using the Pierce LAL Chromogenic Endotoxin Quantitation Kit (Thermo Fisher Scientific, #88282). LPS quantification by ELISA used the LPS ELISA kit from MyBiosource (#MBS700021). For sandwich ELISA to analyze LPS-HDL binding, we used high-binding clear polystyrene microtiter plates (R&D Systems, #DY990), and purified HDL was immobilized for 2 hours on these plates at 37°C at 10 μg/ml. After washing, plates were blocked with 1% BSA for 1 hour. Then biotinylated LPS was preincubated with or without 1 μg/ml of recombinant LBP (R&D Systems) for 1 hour and incubated in plates for 30 min. For ELISA to quantify biotin, samples including biotinylated LPS were incubated in high-binding clear polystyrene microtiter plates overnight at 37°C. Streptavidin peroxidase (R&D Systems) was added, followed by diaminobenzidine substrate (Abcam), for colorimetric reactions. Colorimetric or fluorometric absorbance was detected using the Cytation 5 Cell Imaging Multi-Mode Reader (BioTek).

IP of HDL, LDL, and biotinylated LPS

For proteomic analysis of systemic and portal plasma, human plasma samples were separated using size-exclusion FPLC and then plasma albumin and IgG were depleted using the Pierce Albumin/IgG Removal kit (Thermo Fisher Scientific, #89875). Immunoprecipitation (IP) on the separated HDL fractions was conducted using Pierce MS-Compatible Streptavidin Magnetic IP Kit (Thermo Fisher Scientific, #90408). The anti-human apoA1 antibody (Proteintech, #14427-1) was biotinylated using Pierce Antibody Biotinylation kit for IP (Thermo Fisher Scientific, #90407) for later capture by streptavidin IP. The samples were eluted at low pH and neutralized to 100 mM Tris, pH 8.0.

Biotinylated LPS in cell media was mixed with 1% SDS to disrupt lipoproteins and then purified using Streptavidin Magnetic IP kit. Endotoxin activity of the immunopurified biotinylated LPS was measured using the LAL kit and normalized by relative amount of biotin as detected in ELISA.

For binding studies, 50 μg/ml of protein in HDL_3, HDL_2, or LDL fractions was mixed with 1 μg/ml of LBP and 20 μg/ml of biotinylated LPS in 100 mM NaCl, 100 mM Tris, and 1 mM EDTA buffer for 2 hours. The mixtures were incubated with anti-apoA1 antibody (Proteintech) or anti-apoB antibody (Thermo Fisher Scientific, #MIA1605) overnight and immunoprecipitated using Protein A agarose beads (Abcam, #ab193254). The bead-bound samples were eluted using 0.1 M glycine buffer (pH 2.5) and neutralized using 100 mM Tris, pH 8.0. The distributions of LBP and biotinylated LPS were measured by immunoblotting and streptavidin-peroxidase ELISA, respectively.

Generation of reconstituted HDL (rHDL)

Human apoA1 isolation and purification from fresh human plasma was performed as reported previously (51). The lyophilized protein was solubilized and denatured in STB (10 mM Tris, 0.15 M NaCl, 1 mM EDTA, and 0.2% NaN₃) containing 3 M guanidine HCl, followed by refolding at 4°C by dialyzing against three changes of 4 liters of STB for a minimum of 3 hours each. rHDL particles were generated with a modified sodium cholate dialysis as previously described (52). A molar ratio of 80:1 POPC (Avanti Polar Lipids) and apoA1, respectively, was used to generate rHDL.

Depletion of HDL or AOAH

The HDL in mouse plasma was removed with the HDL Depletion Column IgY Kit (Genway Biotech, #GWB-HDLIGY). AOAH in cell medium was depleted through IP by anti-AOAH antibody (Proteintech) and Protein A agarose beads. After IP, the supernatant was harvested and depletion of HDL or AOAH confirmed by immunoblotting.

Chromatographic analysis of biotinylated LPS transfer between lipoprotein species

HDL_3 or HDL_2 (100 μg protein/ml) was incubated with or without 2 μg/ml of LBP and 1 μg/ml of biotinylated LPS in Tris buffer for 30 min and then dialyzed in a Slide-A-Lyzer Dialysis cassette kit. Isolated VLDL (10 μg/ml of protein) and LDL (50 μg/ml of protein) were subsequently added to the HDL-LPS mixture and incubated for 2 hours at 37°C. The 200-μl mixture was then subjected to FPLC separation using a Superose 6 10/300GL gel filtration column. The amount of biotin was measured through streaptavidin peroxidase ELISA, and lipoprotein-associated LPS was thereby determined.

Portal vein injection of biotinylated LPS and lipoprotein complex

A mixture containing 5 μg of biotinylated LPS and 2 μg of LBP was incubated with 0.1 mg of HDL_3, HDL_2, or LDL (concentration determined by protein not lipid) in saline buffer for 3 hours. Mice were anaesthetized by injection of a mixture of ketamine (50 mg/kg body weight) and xylazine (8 mg/kg body weight) intraperitoneally. The LPS-loaded lipoprotein mixtures described above were then injected through the portal vein in a 100-μl volume using an ultrasmall 33-gauge needle. VETSPON Absorbable Hemostatic Gelatin Sponges (Novartis) were used to stop bleeding of the portal vein. Systemic blood and livers were harvested 30 min later.

Peptide preparation and nano-liquid chromatography–tandem mass spectrometry

Peptides were prepared as previously described (53). Then modification of a previous method (54) was followed. First, the column was equilibrated to 0.1% formic acid (FA) for a total of 11 μl at 700 bar pressure. The samples in FA (1%) were loaded on an EASY nanoLC (Thermo Fisher), with sample (2.5 μl) applied onto a 75-μm inner diameter × 50-cm Acclaim PepMap 100 C18 RSLC column (Thermo Fisher). A constant pressure of 700 bar was maintained at 0.1% FA. Peptide chromatography was performed using mobile phase A (1% FA) containing 2% B (100% MeCN, 1%FA) for 5 min, then increased to 20% B over 100 min, to 32% B over 20 min, to 95% B over 1 min, and held at 95% B for 29 min. The flow rate was 250 nl/min. Data were acquired in data-dependent acquisition (DDA) mode. Full-scan mass spectra were acquired with the Orbitrap mass analyzer with a scan range of m/z = 350 to 1500 and a mass resolving power set to 70,000. Ten data-dependent, high-energy collisional dissociations were performed with a mass-resolving power set to 17,500, a fixed lower value of m/z 100, an isolation width of 2 Da, and a normalized collision energy setting of 27. The maximum injection time was 60 ms for parent ion analysis and product ion analysis. The target ions that were selected for tandem mass spectrometry (MS/MS) were dynamically excluded for 20 s. The automatic gain control was set at a target value of 3×10^{-6} ions for full MS scans and 1×10^{-5} ions for MS2. Peptide ions with charge states of 1 or >8 were excluded for HCD acquisition.

Protein identification

The MS unprocessed data from the mass spectrometer were converted to peak lists using Proteome Discoverer (Thermo Fisher Scientific). The MS2 spectra with charges +2, +3, and +4 were analyzed using Mascot software (Matrix Science). Mascot was set up to search against a UniProt (July 2019) database of human

proteins (20,667 entries), using trypsin cleavage specificity (trypsin/P) with four missed cleavages allowed. The searches were performed using Mascot software according to previously described parameters for peptide identification (*53*). Peptides and proteins were filtered at 1% false discovery rate (FDR) by searching against a reversed protein sequence database. The ontology of HDL signature proteins were acquired from DAVID bioinformatics functional annotation (https://david.ncifcrf.gov/).

RNA sequencing

Three individual mice per experimental group were used for the generation of whole intestinal or whole liver RNA sequencing. Total RNA integrity was determined using an Agilent Technologies Bioanalyzer or 4200 Tapestation. Library preparation was performed with 500 ng to 1 μg of total RNA. Ribosomal RNA was removed by an RNase-H method using RiboErase kits (Kapa Biosystems), and mRNA was then fragmented in reverse transcriptase buffer with heating to 94°C for 8 min. Then mRNA was reverse transcribed to yield cDNA using SuperScript III RT enzyme (Life Technologies) and random hexamers. A second strand reaction was performed to yield ds-cDNA. cDNA was blunt-ended, had an A base added to the 3′ ends, and then had Illumina sequencing adapters ligated to the ends. Ligated fragments were then amplified for 12 to 15 cycles using primers incorporating unique dual index tags. Fragments were sequenced on an Illumina NovaSeq-6000 using paired-end reads extending 150 bases. The gene counts were quantified with CPM transformations added with custom R scripting. Normalized Log2 CPM values were visualized as heatmaps through the web interface Phantasus (https://genome.ifmo.ru/phantasus). Gene ontology pathway analyses were acquired from DAVID bioinformatics functional annotation. The sequencing and expression data have been deposited in the Gene Expression Omnibus (GEO) database of the National Center for Biotechnology Information with the accession number GSE167983.

Human studies

Human portal and peripheral systemic blood was acquired from adult patients undergoing open surgical procedures in which the surgical team deemed that the portal vein was safely accessible. Blood was collected in EDTA-containing tubes and centrifuged for immediate analysis of plasma for HDL. The population of patients from which plasma was acquired was composed of three males and three females ranging in age from 54 to 80. Four underwent Whipple pancreatic surgery, one underwent gastric bypass, and one underwent an orthotopic liver transplant. Immunoblots were performed using tissue specimens from other patients under-

going surgical resection for proximal or distal gut after traumatic injury. These were collected and fixed in formalin by the Department of Pathology and Immunology for a routine surgical pathology workup and were shared for research after sign out of the clinical case. After dissecting tissue enriched in epithelium, dissected tissues were stabilized in PAXgene Tissue Stabilization buffer (PreAnalytiX, #765512) for at least 3 hours. Protein lysates were then prepared by homogenization in Extraction EXB buffer (Qiagen, #37623). All human studies were approved by the Human Research Protection Office at Washington University (institutional review board protocols #201111038 and #2019101009, PI G. J. Randolph).

Statistics

All graphs are plotted to depict mean ± SEM. A paired or unpaired two-tailed Student's t test was used for simple comparisons, a one-way ANOVA with Tukey's post hoc test for multiple comparisons for three or more groups with one variable, or a two-way ANOVA with Sidak post hoc test for three or more groups with two variables. Statistical differences were analyzed and graphs were prepared using GraphPad Prism software version 8.0. $P < 0.05$ was considered to be a significant difference. Replicates in the bar graphs are shown by distinct symbols. Replicates in biochemical and/or binding experiments were independent technical replicates using the same reagents (technical replicates; Figs. 3 and 4, A to F). In other experiments, each symbol in a graph represents experiments where independent cell preparations of plasma (Fig. 1, A and F, and Fig. 2, A and B; paired samples) or primary cells (Fig. 3, A to E, and Fig. 4, G to L) were generated and studied within the experimental design. Finally, in all in vivo experiments, each symbol in a graph represents data generated from an individual mouse (Fig. 1, C to E; Fig. 4M; Fig. 5, A, C, and E to H; Fig. 5, J to L; Fig. 6, A to F, H to J, and L and M; and Fig. 7, A to K). All data using mice contained at least two mice in each experimental group from the same litter, so that the data in a given experimental cohort contained littermate controls in the other groups of the same experiment. Some studies combined mice from three or four litters to generate sufficient numbers. If these mice were subjected to experimental manipulations such as short bowel surgery on different dates, then we refer to the combination of those data into one graph as combining different experiments, with each distinct start date of the experimental manipulation considered an independent experiment. Experimental manipulations that began on the same day with age-matched litters were not classified as independent experiments. The distribution of data was not affected by combining independent experiments. Where possible, data collected

from different experiments were subjected to assays simultaneously to minimize batch effects.

REFERENCES AND NOTES

1. A. Albillos, A. de Gottardi, M. Rescigno, The gut-liver axis in liver disease: Pathophysiological basis for therapy. *J. Hepatol.* **72**, 558–577 (2020). doi: 10.1016/j.jhep.2019.10.003; pmid: 31622696
2. Y. Duan *et al.*, Bacteriophage targeting of gut bacterium attenuates alcoholic liver disease. *Nature* **575**, 505–511 (2019). doi: 10.1038/s41586-019-1742-x; pmid: 31723265
3. R. F. Schwabe, E. Seki, D. A. Brenner, Toll-like receptor signaling in the liver. *Gastroenterology* **130**, 1886–1900 (2006). doi: 10.1053/j.gastro.2006.01.038; pmid: 16697751
4. J. Todoric *et al.*, Fructose stimulated de novo lipogenesis is promoted by inflammation. *Nat. Metab.* **2**, 1034–1045 (2020). doi: 10.1038/s42255-020-0261-2; pmid: 32839596
5. I. Hritz *et al.*, The critical role of toll-like receptor (TLR) 4 in alcoholic liver disease is independent of the common TLR adapter MyD88. *Hepatology* **48**, 1224–1231 (2008). doi: 10.1002/hep.22470; pmid: 18792393
6. L. K. Barron *et al.*, Toll-like receptor 4 is critical for the development of resection-associated hepatic steatosis. *J. Pediatr. Surg.* **52**, 1014–1019 (2017). doi: 10.1016/j.jpedsurg.2017.03.026; pmid: 28351520
7. S. Inokuchi *et al.*, Toll-like receptor 4 mediates alcohol-induced steatohepatitis through bone marrow-derived and endogenous liver cells in mice. *Alcohol. Clin. Exp. Res.* **35**, 1509–1518 (2011). doi: 10.1111/j.1530-0277.2011.01487.x; pmid: 21463341
8. D. M. Levine, T. S. Parker, T. M. Donnelly, A. Walsh, A. L. Rubin, In vivo protection against endotoxin by plasma high density lipoprotein. *Proc. Natl. Acad. Sci. U.S.A.* **90**, 12040–12044 (1993). doi: 10.1073/pnas.90.24.12040; pmid: 8265667
9. M. M. Wurfel, E. Hailman, S. D. Wright, Soluble CD14 acts as a shuttle in the neutralization of lipopolysaccharide (LPS) by LPS-binding protein and reconstituted high density lipoprotein. *J. Exp. Med.* **181**, 1743–1754 (1995). doi: 10.1084/jem.181.5.1743; pmid: 7536794
10. O. Meilhac, S. Tanaka, D. Couret, High-density lipoproteins are bug scavengers. *Biomolecules* **10**, 598 (2020). doi: 10.3390/biom10040598; pmid: 32290632
11. H. G. Windmueller, P. N. Herbert, R. I. Levy, Biosynthesis of lymph and plasma lipoprotein apoproteins by isolated perfused rat liver and intestine. *J. Lipid Res.* **14**, 215–223 (1973). doi: 10.1016/S0022-2275(20)36909-1; pmid: 4349053
12. L. R. Brunham *et al.*, Intestinal ABCA1 directly contributes to HDL biogenesis in vivo. *J. Clin. Invest.* **116**, 1052–1062 (2006). doi: 10.1172/JCI27352; pmid: 16543947
13. C. Martel *et al.*, Lymphatic vasculature mediates macrophage reverse cholesterol transport in mice. *J. Clin. Invest.* **123**, 1571–1579 (2013). doi: 10.1172/JCI63685; pmid: 23524964
14. H. Y. Lim *et al.*, Lymphatic vessels are essential for the removal of cholesterol from peripheral tissues by SR-BI-mediated transport of HDL. *Cell Metab.* **17**, 671–684 (2013). doi: 10.1016/j.cmet.2013.04.002; pmid: 23663736
15. L. H. Huang *et al.*, Interleukin-17 drives interstitial entrapment of tissue lipoproteins in experimental psoriasis. *Cell Metab.* **29**, 475–487.e7 (2019). doi: 10.1016/j.cmet.2018.10.006; pmid: 30415924
16. G. J. Randolph, N. E. Miller, Lymphatic transport of high-density lipoproteins and chylomicrons. *J. Clin. Invest.* **124**, 929–935 (2014). doi: 10.1172/JCI71610; pmid: 24590278
17. R. M. Glickman, P. H. R. Green, The intestine as a source of apolipoprotein A1. *Proc. Natl. Acad. Sci. U.S.A.* **74**, 2569–2573 (1977). doi: 10.1073/pnas.74.6.2569; pmid: 196292
18. W. S. Davidson *et al.*, Proteomic analysis of defined HDL subpopulations reveals particle-specific protein clusters: Relevance to antioxidative function. *Arterioscler. Thromb. Vasc. Biol.* **29**, 870–876 (2009). doi: 10.1161/ATVBAHA.109.186031; pmid: 19325143
19. A. N. Hoofnagle, J. W. Heinecke, Lipoproteomics: Using mass spectrometry-based proteomics to explore the assembly, structure, and function of lipoproteins. *J. Lipid Res.* **50**, 1967–1975 (2009). doi: 10.1194/jlr.R900015-JLR200; pmid: 19738003
20. J. K. Ryu *et al.*, Reconstruction of LPS transfer cascade reveals structural determinants within LBP, CD14, and TLR4-MD2 for efficient LPS recognition and transfer. *Immunity* **46**, 38–50 (2017). doi: 10.1016/j.immuni.2016.11.007; pmid: 27986454
21. C. L. Scott *et al.*, Bone marrow-derived monocytes give rise to self-renewing and fully differentiated Kupffer cells. *Nat. Commun.* **7**, 10321 (2016). doi: 10.1038/ncomms10321; pmid: 26813785

22. J. S. Seidman et al., Niche-specific reprogramming of epigenetic landscapes drives myeloid cell diversity in nonalcoholic steatohepatitis. Immunity 52, 1057–1074 (2020). doi: 10.1016/j.immuni.2020.04.001; pmid: 32362324

23. C. O. Odeyale, Y. H. Kang, Biotinylation of bacterial lipopolysaccharide and its applications to electron microscopy. J. Histochem. Cytochem. 36, 1131–1137 (1988). doi: 10.1177/36.9.3136207; pmid: 3136207

24. J. M. Luk, A. Kumar, R. Tsang, D. Staunton, Biotinylated lipopolysaccharide binds to endotoxin receptor in endothelial and monocytic cells. Anal. Biochem. 232, 217–224 (1995). doi: 10.1006/abio.1995.0010; pmid: 8747478

25. T. Massamiri, P. S. Tobias, L. K. Curtiss, Structural determinants for the interaction of lipopolysaccharide binding protein with purified high density lipoproteins: Role of apolipoprotein A-I. J. Lipid Res. 38, 516–525 (1997). doi: 10.1016/S0022-2275(20)37259-X; pmid: 9101432

26. R. S. Munford, J. P. Weiss, M. Lu, Biochemical transformation of bacterial lipopolysaccharides by acyloxyacyl hydrolase reduces host injury and promotes recovery. J. Biol. Chem. 295, 17842–17851 (2020). doi: 10.1074/jbc.REV120.015254; pmid: 33454018

27. C. M. Courtney, B. W. Warner, Pediatric intestinal failure-associated liver disease. Curr. Opin. Pediatr. 29, 363–370 (2017). doi: 10.1097/MOP.0000000000000484; pmid: 28333693

28. E. J. Onufer et al., Effects of high-fat diet on liver injury after small bowel resection. J. Pediatr. Surg. 55, 1099–1106 (2020). doi: 10.1016/j.jpedsurg.2020.02.037; pmid: 32164985

29. I. Spadoni et al., A gut-vascular barrier controls the systemic dissemination of bacteria. Science 350, 830–834 (2015). doi: 10.1126/science.aad0135; pmid: 26564856

30. M. Sakai et al., Liver-derived signals sequentially reprogram myeloid enhancers to initiate and maintain Kupffer cell identity. Immunity 51, 655–670.e8 (2019). doi: 10.1016/j.immuni.2019.09.002; pmid: 31587991

31. Y. E. Cho, L. R. Yu, M. A. Abdelmegeed, S. H. Yoo, B. J. Song, Apoptosis of enterocytes and nitration of junctional complex proteins promote alcohol-induced gut leakiness and liver injury. J. Hepatol. 69, 142–153 (2018). doi: 10.1016/j.jhep.2018.02.005; pmid: 29458168

32. J. Mouries et al., Microbiota-driven gut vascular barrier disruption is a prerequisite for non-alcoholic steatohepatitis development. J. Hepatol. 71, 1216–1228 (2019). doi: 10.1016/j.jhep.2019.08.005; pmid: 31419514

33. L. R. Brunham et al., Tissue-specific induction of intestinal ABCA1 expression with a liver X receptor agonist raises plasma HDL cholesterol levels. Circ. Res. 99, 672–674 (2006). doi: 10.1161/01.RES.0000244014.19589.8e; pmid: 16946132

34. G. Lo Sasso et al., Intestinal specific LXR activation stimulates reverse cholesterol transport and protects from atherosclerosis. Cell Metab. 12, 187–193 (2010). doi: 10.1016/j.cmet.2010.07.002; pmid: 20674863

35. B. Shao, R. S. Munford, R. Kitchens, A. W. Varley, Hepatic uptake and deacylation of the LPS in bloodborne LPS-lipoprotein complexes. Innate Immun. 18, 825–833 (2012). doi: 10.1177/1753425912442431; pmid: 22441700

36. C. Grunfeld et al., Lipoproteins inhibit macrophage activation by lipoteichoic acid. J. Lipid Res. 40, 245–252 (1999). doi: 10.1016/S0022-2275(20)33363-0; pmid: 9925653

37. Y. Haberman et al., Pediatric Crohn disease patients exhibit specific ileal transcriptome and microbiome signature. J. Clin. Invest. 124, 3617–3633 (2014). doi: 10.1172/JCI75436; pmid: 25003194

38. S. S. Martin et al., HDL cholesterol subclasses, myocardial infarction, and mortality in secondary prevention: The Lipoprotein Investigators Collaborative. Eur. Heart J. 36, 22–30 (2015). doi: 10.1093/eurheartj/ehu264; pmid: 24980493

39. J. J. Albers, A. Slee, J. L. Fleg, K. D. O'Brien, S. M. Marcovina, Relationship of baseline HDL subclasses, small dense LDL and LDL triglyceride to cardiovascular events in the AIM-HIGH clinical trial. Atherosclerosis 251, 454–459 (2016). doi: 10.1016/j.atherosclerosis.2016.06.019; pmid: 27320173

40. G. Gracia, E. Cao, A. P. R. Johnston, C. J. H. Porter, N. L. Trevaskis, Organ-specific lymphatics play distinct roles in regulating HDL trafficking and composition. Am. J. Physiol. Gastrointest. Liver Physiol. 318, G725–G735 (2020). doi: 10.1152/ajpgi.00340.2019; pmid: 32068443

41. G. P. Forester, A. R. Tall, C. L. Bisgaier, R. M. Glickman, Rat intestine secretes spherical high density lipoproteins. J. Biol. Chem. 258, 5938–5943 (1983). doi: 10.1016/S0021-9258(20)81987-5; pmid: 6853560

42. H. R. Bearnot, R. M. Glickman, L. Weinberg, P. H. Green, A. R. Tall, Effect of biliary diversion on rat mesenteric lymph apolipoprotein-I and high density lipoprotein. J. Clin. Invest. 69, 210–217 (1982). doi: 10.1172/JCI110432; pmid: 6798073

43. H. C. Oliveira, K. Nilausen, H. Meinertz, E. C. Quintão, Cholesteryl esters in lymph chylomicrons: Contribution from high density lipoprotein transferred from plasma into intestinal lymph. J. Lipid Res. 34, 1729–1736 (1993). doi: 10.1016/S0022-2275(20)35735-7; pmid: 8245723

44. E. C. Quintão, A. Drewiacki, K. Stechhaln, E. C. de Faria, A. M. Sipahi, Origin of cholesterol transported in intestinal lymph: Studies in patients with filarial chyluria. J. Lipid Res. 20, 941–951 (1979). doi: 10.1016/S0022-2275(20)39995-8; pmid: 533829

45. I. Pierantonelli et al., HDL cholesterol protects from liver injury in mice with intestinal specific LXRα activation. Liver Int. 40, 3127–3139 (2020). doi: 10.1111/liv.14712; pmid: 33098723

46. T. Yasuda et al., Tissue-specific liver X receptor activation promotes macrophage reverse cholesterol transport in vivo. Arterioscler. Thromb. Vasc. Biol. 30, 781–786 (2010). doi: 10.1161/ATVBAHA.109.195693; pmid: 20110577

47. B. Wang, P. Tontonoz, Liver X receptors in lipid signalling and membrane homeostasis. Nat. Rev. Endocrinol. 14, 452–463 (2018). doi: 10.1038/s41574-018-0037-x; pmid: 29904174

48. S. Daemen et al., Dynamic shifts in the composition of resident and recruited macrophages influence tissue remodeling in NASH. Cell Rep. 34, 108626 (2021). doi: 10.1016/j.celrep.2020.108626; pmid: 33440159

49. F. Guo, K. Zheng, R. Benedé-Ubieto, F. J. Cubero, Y. A. Nevzorova, The Lieber-DeCarli diet: A flagship model for experimental alcoholic liver disease. Alcohol. Clin. Exp. Res. 42, 1828–1840 (2018). doi: 10.1111/acer.13840; pmid: 30025151

50. Y. H. Han et al., RORα induces KLF4-mediated M2 polarization in the liver macrophages that protect against nonalcoholic steatohepatitis. Cell Rep. 20, 124–135 (2017). doi: 10.1016/j.celrep.2017.06.017; pmid: 28683306

51. W. S. Davidson, G. M. Hilliard, The spatial organization of apolipoprotein A-I on the edge of discoidal high density lipoprotein particles: A mass specrometry study. J. Biol. Chem. 278, 27199–27207 (2003). doi: 10.1074/jbc.M302764200; pmid: 12724319

52. E. A. Bonomo, J. B. Swaney, A rapid method for the synthesis of protein-lipid complexes using adsorption chromatography. J. Lipid Res. 29, 380–384 (1988). doi: 10.1016/S0022-2275(20)38530-8; pmid: 3132520

53. J. Rustenhoven et al., Functional characterization of the dural sinuses as a neuroimmune interface. Cell 184, 1000–1016. e27 (2021). doi: 10.1016/j.cell.2020.12.040; pmid: 33508229

54. D. Patra, J. Kim, Q. Zhang, E. Tycksen, L. J. Sandell, Site-1 protease ablation in the osterix-lineage in mice results in bone marrow neutrophilia and hematopoietic stem cell alterations. Biol. Open 9, bio052993 (2020). doi: 10.1242/bio.052993; pmid: 32576566

Science

Enterically derived high-density lipoprotein restrains liver injury through the portal vein

Yong-Hyun HanEmily J. OnuferLi-Hao HuangRobert W. SprungW. Sean DavidsonRafael S. CzepielewskiMary WohltmannMary G. Sorci-ThomasBrad W. WarnerGwendalyn J. Randolph

Intestinal HDL is hepatoprotective

High-density lipoprotein (HDL) is important for cholesterol metabolism and may have anti-inflammatory and antimicrobial properties. Although HDL is mainly produced by the liver, the intestine is also a source. Han *et al.* show in mice that intestinal HDL is not routed to the systemic circulation. Rather, in the form of HDL3, it is directly transported to the liver through the hepatic portal vein. There, it sequesters bacterial lipopolysaccharide from the gut that can trigger inflammation and liver damage. In various models of liver injury, loss of enteric HDL exacerbated pathology. By contrast, drugs elevating intestinal HDL improved disease outcomes. HDL3 is enriched in human portal venous blood, suggesting that enteric HDL may be targetable for the treatment of liver disease.

View the article online
https://www.science.org/doi/10.1126/science.abe6729
Permissions
https://www.science.org/help/reprints-and-permissions

Use of think article is subject to the Terms of service